Università degli studi di Padova

SCUOLA DI SCIENZE
DIPARTIMENTO DI FISICA E ASTRONOMIA
"GALILEO GALILEI"

Tesi di Laurea Magistrale in Astronomia

DETERMINING THE PROGENITORS OF MERGING BLACK HOLE BINARIES WITH GENERAL RELATIVISTIC GALAXY CORRELATIONS

Relatore:
Prof. SABINO MATARRESE

Correlatori:
Dott. ALVISE RACCANELLI
Prof. LICIA VERDE

Laureando:
GIULIO SCELFO
Matricola 1131500

Anno Accademico 2017-2018

Abstract *The detection of binary black hole mergers through gravitational waves by the LIGO-Virgo instrument sparked the discussion on whether they have astrophysical or primordial origin. According to a currently popular model, primordial black holes of stellar mass could constitute a relevant fraction of the dark matter. This work aims to forecast the possibility to infer the nature of the binary black hole progenitors through cross-correlations between galaxy catalogs and gravitational wave maps.*

Introduction

It is undeniable that gravitational wave astronomy has opened a new door to scientific research. The breakthrough announcement by the LIGO team of the first detection of gravitational waves on September 2015, emitted by two merging black holes of $\sim 30M_{\odot}$, not only confirmed one of the predictions of General Relativity, but most of all established the birth of a new way to observe and analyze the cosmos.
Thanks to gravitational waves detection, we are now able to receive information from binary black holes systems in coalescence. The fact that most of them have progenitors of masses between 20 and 40 $M_{\odot}$ opened up the interest towards the hypothesis that these black holes may have primordial origin and that they could even constitute a significant part of the dark matter we are looking for.
Primordial black holes are hypothetical objects who are thought to be formed during the early universe because of large density fluctuations that could start gravitational collapse, from which a black hole formation can take place. In addition, there are no valid constraints that exclude the possibility that primordial black holes in the mass range mentioned above could exist in significant quantity. It is also worth noticing that studying primordial black holes would still be useful even if they did not compose a major percentage of the dark matter. In fact, their abundance could provide constraints to early universe models and they could also be plausible candidates of seeds of super massive black holes existing at the center of large galaxies.
This project aims to analyze one current model of "primordial black holes as dark matter" and forecast the possibility for near future survey to test its validity. The work is organized as follows.
In Chapter 1 some background introductory notions about cosmology and gravitational waves are provided, so that this work can be self-consistent in every notion.
In Chapter 2 we give some basic concepts about primordial black holes formation and constraints, explaining why it is possible to say that those in the mass range detected by gravitational waves experiments could still survive today in significant quantities.
At this point, in Chapter 3 we present a model according to which primordial black holes of masses of approximately $30M_{\odot}$ could make up dark matter. We describe in detail all the assumptions made, stressing that this model provides an estimate of the black holes merger rate which is consistent with that given by the LIGO team.
One of the basic concepts of the scientific method is that a theory has to give the possibility to be tested. This is what we address in Chapter 4, where we explain a method to verify or falsify the "$30M_{\odot}$ primordial black holes as dark matter" theory. This is based on

cross-correlating gravitational wave events with star forming galaxy maps, aiming to infer if the merging black holes detected have primordial or stellar origins. Since for the moment we do not have a large map of gravitational waves events to analyze, what we did is forecast if future surveys will have enough capabilities to accomplish it. It is possible to develop this kind of forecast through the Fisher matrix approach, which we also describe here.
Then, in Chapter 5 we explain in detail the methodology and assumptions made for this work. We applied the Fisher analysis to the data coming from the number counts cross-correlation power spectrum between our two tracers. In this way, we can infer if future surveys will be able to verify the validity of the "primordial black holes as dark matter" theory. In addition, in this Chapter we also show how we derived an expression for the magnification bias of gravitational waves sources, in analogy to the one of luminous objects. In Chapter 6 we present our results, affirming that near future surveys will indeed be able to test the validity of this "primordial black holes as dark matter" theory. We also show that the cosmic magnification effects have a strong influence on the results.
Finally, in Chapter 7 we sum up our conclusions.

Contents

Chapter 1

Introductive cosmology topics

One of the basis of Cosmology is the so called Cosmological Principle. It states that the Universe is homogeneous and isotropic at large scales. Homogeneity and isotropy imply that there are no preferred locations or directions respectively, therefore every observer will measure on average the same properties of the Universe in every point of the space and looking in any direction. Even though at small scales the Universe is inhomogeneous, the validity of this principle on larger scales was confirmed by many experiments studying the Large Scale Structures of the Universe and the Cosmic Microwave Background. The latter one is a black body radiation constituted by photons having an average temperature of $T_{\mathrm{CMB}} \simeq 2.7K$ and is a relic of the first times of the Universe, when it was still opaque. When it became transparent at hydrogen recombination time, approximately 380000 years after the Big Bang, these photons were free to travel and are observed today. The fact that its relative temperature fluctuations are of the order of only $\delta T/T \simeq 10^{-5}$ in every direction of the sky is a strong evidence of isotropy and homogeneity.
At the moment, the model that best fits our cosmological observational data and is able to make robust predictions is the Λ-Cold Dark Matter model (ΛCDM). To our knowledge, the ingredients composing the content of matter-energy of the Universe are those listed below. The abundance of a certain species can be expressed using the density parameter $\Omega \equiv \rho/\rho_c$, where ρ is the density of the specie and and ρ_c the critical density, i.e. the density necessary to have a flat space. According to the ΛCDM model, our Universe today is made of:

- *Baryonic Matter* ($\Omega_b \simeq 0.05$): this is the ordinary matter made of electrons, protons and neutrons. They started forming the first atomic nuclei in the early Universe (during the Nucleosynthesis);

- *Cold Dark Matter* ($\Omega_{\mathrm{cdm}} \simeq 0.26$): this is a percentage of matter whose nature we do not know yet and that may be made of non-baryonic constituents. It does not interact with radiation, so we call it dark. The term "cold" derives from the fact that this specie decoupled from the other components when its particles were not relativistic. We give more detail about the dark matter problem in Section 1.1.5;

- *Dark Energy* ($\Omega_\Lambda \simeq 0.71$): this energy component had to be introduced to justify the fact that the Universe in expanding in an accelerated way (which, for example,

can be argued by observing Type Ia Supernovae). In the most common framework dark energy is the famous cosmological constant (Λ) introduced by Einstein but some alternative theories hypothesized that this prescription could indeed be not true;

- *Radiation* ($\Omega_r \simeq 10^{-5}$). The radiation component of the Universe (i.e. photons) gives a very low contribution to the total energy today, but was once dominating in the early stages of the Universe, during the so called radiation dominated era.

To quantify the total matter abundance, the parameter

$$\Omega_m = \Omega_{\rm cdm} + \Omega_b \tag{1.1}$$

is often used.
Given some basic information about the general framework regarding our Universe, in the rest of this chapter we shall provide some other background concepts about Cosmology and Gravitational Wave physics that were used during this work.

1.1 Description of the Universe

1.1.1 Robertson-Walker metric

When approaching to the study of the Universe, one of the most important issue is being able to determine how to measure distances between two points in the space-time. To do so, we have to establish a rule, which is given by the geometry of the space considered, described by the line element ds^2 from the assumed metric $g_{\mu\nu}$. The simplest type of metric that one could think of is the Minkowski one:

$$\eta_{\mu\nu} = diag(-1, 1, 1, 1) \tag{1.2}$$

and the corresponding line element ds^2 reads as

$$ds^2 = -(c\,dt)^2 + dx^2 + dy^2 + dz^2 \tag{1.3}$$

in Cartesian coordinates, and

$$ds^2 = -(c\,dt)^2 + dr^2 + r^2 d\theta^2 + r^2 \sin^2\theta d\phi^2 \tag{1.4}$$

in the polar coordinates

$$\begin{cases} x = r\sin\theta\cos\phi \\ y = r\sin\theta\sin\phi \\ z = r\cos\theta \end{cases} \tag{1.5}$$

where c is the speed of light.
Following the cosmological principle, H. Robertson and A. Walker derived the expression

for the metric of a spatially homogeneous and isotropic Universe. This metric, called Robertson-Walker metric, can be written as [1]:

$$ds^2 = -dt^2 + a(t)^2\left[\frac{dr^2}{1-kr^2} + r^2 d\Omega^2\right], \tag{1.6}$$

where $d\Omega = d\theta^2 + \sin^2\theta d\phi^2$. The constant k depends on the curvature of the space-like hypersurfaces time: it is $k = 0$ for the case of flat space, $k > 0$ for a closed space and $k < 0$ for an open space. A variable rescaling is often applied, such that k can only assume the values $k = -1; 0; 1$. The time t is the so called cosmological proper time: it is the time measured by a reference frame who sees the Universe expanding uniformly around him. The spatial coordinates (r, θ, ϕ) are said to be comoving of a point in space. It means that, if the Universe expands homogeneously and isotropically, these coordinates remain fixed over time. Finally, $a(t)$ is the so called scale factor. It relates comoving distances with the physical ones such that

$$d_{\text{physical}} = a(t)\, d_{\text{comoving}} \tag{1.7}$$

with the normalization of $a(t) = 1$ today.
Note the the RW metric is appropriate only when describing the Universe on large scales: at small ones, instead, it is not homogeneous and another metric has to be considered.

1.1.2 Evolution equations

Let's now introduce the Einstein equations. They relate the geometry of the space-time with the matter-energy that influences it as:

$$R_{\mu\nu} - \frac{1}{2}Rg_{\mu\nu} = 8\pi G T_{\mu\nu} \tag{1.8}$$

where $R_{\mu\nu}$ (Ricci tensor) and $R = R^{\mu}_{\mu}$ (Ricci scalar) provide information about the geometry, while $T_{\mu\nu}$ is the energy-momentum tensor. G is the universal gravitational constant. In the case of a perfect fluid, the energy-momentum tensor assumes the following expression:

$$T^{\mu\nu} = (\rho + p)u^{\mu}u^{\nu} + pg^{\mu\nu} \tag{1.9}$$

where ρ, p, u^{μ} are the matter-energy density, the isotropic pressure and the 4-velocity of the fluid. For a reference frame at rest with the fluid it reduces to

$$T^{\mu\nu} = \text{diag}(\rho, p, p, p). \tag{1.10}$$

Then, assuming the cosmological fluid as perfect and considering that on large scales our Universe can be described by a RW metric, we can obtain the so called Friedmann equations by computing the Einstein equations:

$$\begin{cases} H^2 = \left(\dfrac{\dot{a}}{a}\right)^2 = \dfrac{8}{3}\pi G\rho - \dfrac{kc^2}{a^2} \\ \dfrac{\ddot{a}}{a} = -\dfrac{4}{3}\pi G\left(\rho + \dfrac{3p}{c^2}\right) \end{cases} \tag{1.11}$$

where we have omitted to specify time dependences and where $\cdot$ indicates a derivative respect to t. These equations are essential in describing the background dynamics of our Universe, since they describe how the scale factor $a(t)$ varies with time.
From the first Friedmann equation an expression for the critical density ρ_c that would correspond to a flat Universe ($k = 0$) can be provided. It yields:

$$\rho_c = \frac{3H^2}{8\pi G}. \tag{1.12}$$

We can introduce the parameter Ω_k which describes the geometry of the universe in the following way:

$$\Omega_k + \Omega_m + \Omega_\Lambda + \Omega_r = 1, \tag{1.13}$$

meaning that:

- $\Omega_k = 0$ for a flat Universe;
- $\Omega_k < 0$ for a closed Universe;
- $\Omega_k > 0$ for an open Universe.

As of today, experiments tell us that $|\Omega_k| < 0.005$ [2].

Another important equation is the continuity equation, which derives from the Bianchi identities (that yield $T^{\mu\nu}_{;\nu} = 0$) and describes the energy density evolution of the cosmic fluid in a Universe described by the RW metric. It states that

$$\dot{\rho} + 3H(\rho + p) = 0. \tag{1.14}$$

Another useful expression which relates p with ρ, providing us with the third of three independent equations in the unknowns a, ρ, p, is the equation of state:

$$p = w\rho \tag{1.15}$$

where w is a constant.
From the continuity equation we can obtain that $\rho \sim a^{-3(1+w)}$ which brings to

$$a(t) = t^{\frac{2}{3}(1+w)}. \tag{1.16}$$

For a matter domination Universe the equation of state is $w = 1/3$, from which

$$\rho \sim a^{-4} \quad ; \quad a(t) \sim t^{1/2}, \tag{1.17}$$

while for non-collisional matter domination we have that $w = 0$ and then

$$\rho \sim a^{-3} \quad ; \quad a(t) \sim t^{2/3}. \tag{1.18}$$

1.1.3 Distance measurements

In cosmology there are different ways to measure distances between two points. We shall expose them in this Section. Firstly, let's introduce the Hubble constant H_0. It expresses the proportionality between the recession speed v and the distance d of an object from the observer:

$$v = H_0 d. \tag{1.19}$$

The above expression, known as Hubble law, was first theoretically proposed by Lemaitre and then experimentally observed by Hubble [3], looking at close galaxies, by measuring their redshift z. The redshift z was obtained by the looking at the shift in the galaxies spectral lines. It can be quantified as:

$$z = \frac{f_e}{f_o} - 1 = \sqrt{\frac{1 + v/c}{1 - v/c}} - 1 \approx \frac{v}{c}, \tag{1.20}$$

where f_e and f_o are the emitted and observed frequencies of the light emitted from the sources. Note that this expression is valid only for nearby objects ($v \ll c$), a general description of the redshift is in fact given by relativity. Some calculus can provide a relation between redshift and scale factor: $a(t) = (1 + z)^{-1}$.
In Figure 1.1 we provide the original Hubble diagram, published after this discovery.

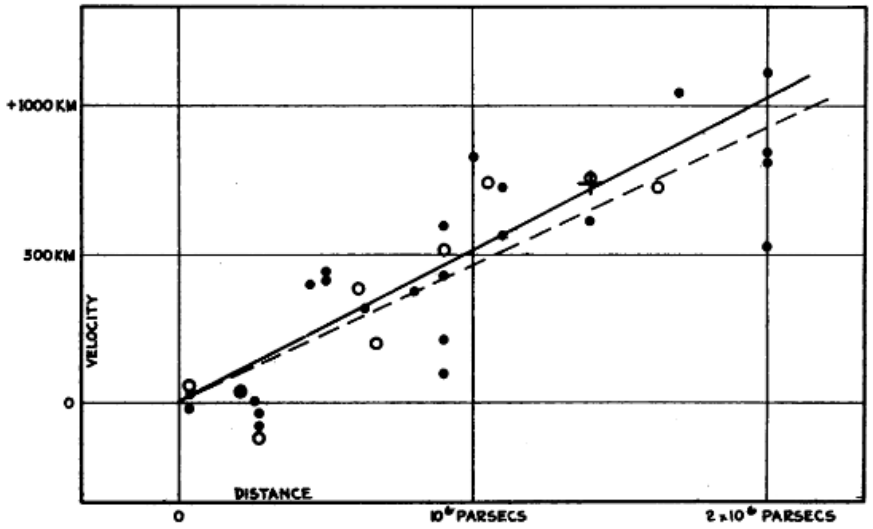

Figure 1.1: Hubble diagram from the original paper [3]. Note that the vertical axes provides velocity measurements and not distances, as erroneously written. It is evident that the galaxy velocities increase with distance from the observer.

It must be specified that the value H_0 is only valid today. In fact, generally one has to consider the Hubble parameter $H(t)$, which varies with time. Measurements of the Hubble constant by the Planck mission [2] provide the value of

$$H_0 = 67.08 \pm 0.9\, km/s/Mpc. \tag{1.21}$$

In cosmology it is also often used the parameter h, which is H_0 in units of $100\,km/s/Mpc$. It is worth mentioning that an issue regarding the value of this constant is still open, since local measurements of H_0 (e.g. based on standard candles) yield values typically higher than those based on non-local methods (e.g. observing the Cosmic Microwave Background) [4].
From this constant it is possible to determine the so called Hubble time t_H:

$$t_H = \frac{c}{H_0} = 9.78 \cdot 10^9\, h^{-1}\, yr, \tag{1.22}$$

which gives a rough estimate of the age of the Universe, and the Hubble distance d_H:

$$d_H \equiv \frac{c}{H_0} = 3000\, h^{-1} Mpc, \tag{1.23}$$

which sets the scale of the Universe, since it can be seen as the distance traveled by light in a Hubble time.
Defining

$$E(z) = \sqrt{\Omega_m (1+z)^3 + \Omega_k (1+z)^2 + \Omega_\Lambda}, \tag{1.24}$$

the Hubble parameter can be written as $H(z) = H_0 E(z)$ and we can introduce the line-of-sight comoving distance $\chi(z)$:

$$\chi = d_H \int_0^z \frac{dz'}{E(z')}. \tag{1.25}$$

From this, it is possible to derive the comoving transverse distance d_M between two objects at the same redshift but located in different points on the sky. It reads as:

$$d_M \equiv \begin{cases} d_H \dfrac{1}{\sqrt{\Omega_k}} \sinh\left[\sqrt{\Omega_k}\chi/d_H\right] & \text{for } \Omega_\mathrm{k} > 0; \\ \chi & \text{for } \Omega_\mathrm{k} = 0; \\ d_H \dfrac{1}{\sqrt{\Omega_k}} \sin\left[\sqrt{\Omega_k}\chi/d_H\right] & \text{for } \Omega_\mathrm{k} < 0. \end{cases} \tag{1.26}$$

The angular diameter distance d_A, instead, is given by the ratio of the physical transverse dimension of on object and its and its angular size in radians. It can be expressed as

$$d_A \equiv \frac{d_M}{1+z}. \tag{1.27}$$

Then, we can define the luminosity distance d_L as

$$d_L \equiv \sqrt{\frac{L}{4\pi S}}, \tag{1.28}$$

where S is the bolometric flux of the object and L its bolometric luminosity. It can also be expressed in function of the other types of distances seen before:

$$d_L = (1+z) d_M = (1+z)^2 d_A. \tag{1.29}$$

Finally, we provide the expression of the comoving volume, which gives the measure of a volume in which the number densities of non-evolving sources following the Hubble expansion are constant with redshift. For a redshift interval dz and a solid angle $d\Omega$ the comoving volume element is

$$dV_c = D_H \frac{(1+z)^2 D_A^2}{E(z)} d\Omega dz. \tag{1.30}$$

We conclude providing here the expression for a quantity that will be mentioned in this work. We can define the particle horizon $D_H(t)$ as the radius of the sphere containing all the portions of the Universe that could have been in causal contact with an observer (positioned in the sphere center) up to the time t. It is given by:

$$D_{\rm H}(t) = a(t) \int_0^t \frac{cdt'}{a(t')}. \tag{1.31}$$

It is obtained by imposing that the RW metric line element $ds^2 = 0$, which is valid for photons.

1.1.4 Power spectrum

Let's consider a generic fluctuation $\delta(x,t)$ in a point of the space-time. For example, it can be the fluctuation of the density field. It is useful to introduce the following statistical tool [1]:

$$\xi(r) = \langle \delta(x+r,t)\delta(x,t) \rangle \tag{1.32}$$

called two-point correlation function. It is an average value taken over the entire statistical ensemble. In the Fourier space we can write

$$\delta(x,t) = \frac{1}{(2\pi)^3} \int d^3k e^{ik\,x} \delta_k(t) \tag{1.33}$$

and define the power spectrum $\mathcal{P}(k)$ of the fluctuation δ as:

$$\langle \delta_{k_1} \delta_{k_2} \rangle = (2\pi)^3 \mathcal{P}(k) \delta^{(3)}(k_1 + k_2). \tag{1.34}$$

It is straightforward to show that the power spectrum is the Fourier transform of the two-point correlation function. In fact, considering the expansion in plane waves:

$$\begin{aligned} \xi(r) = \langle \delta(x+r)\delta(x) \rangle &= \left\langle \frac{1}{(2\pi)^3} \int d^3k e^{ik\,x} \delta_k \frac{1}{(2\pi)^3} \int d^3k' e^{ik'\,x} \delta'_k \right\rangle \\ = \int \frac{d^3k}{(2\pi)^3} \int \frac{d^3k'}{(2\pi)^3} e^{ik\,(x+r)} e^{ik'\,x} (2\pi)^3 \mathcal{P}(k) \delta^{(3)}(k+k') &= \int d^3k (2\pi)^3 \mathcal{P}(k) e^{ik\,r}. \end{aligned} \tag{1.35}$$

Finally, introducing the variance $\sigma^2 = \langle \delta^2(x) \rangle$, it is possible to show that another way to express the power spectrum is

$$\Delta(k) = \frac{k^3}{2\pi^2} \mathcal{P}(k) \tag{1.36}$$

where

$$\sigma^2 = \int_0^\infty \frac{dk}{k} \Delta(k). \tag{1.37}$$

1.1.5 Dark Matter Problem

According to the ΛCDM model, about 27 % of the energy content of the Universe seems to be made of the so called dark matter, a type of matter that does not interact with light and, therefore, is not directly visible with our instruments. Historically, one of the first reasons that led to introduce this component came from the observations of galaxy velocity curves.
Consider a star moving in an approximately circular orbit around the center of its host galaxy, with a velocity v and a distance R from the galactic center. It will be subject to the acceleration

$$a_g = \frac{v^2}{R} \tag{1.38}$$

toward the center. Considering that a_g is caused by the gravitational attraction to the galaxy, we can write

$$a_g = \frac{GM(R)}{R^2} \tag{1.39}$$

where $M(R)$ is the mass inside the radius R. From the equality of the above two expression we get

$$v = \sqrt{\frac{GM(R)}{R}}. \tag{1.40}$$

The velocities v are measurable experimentally, and can then be compared with the prediction of Equation (1.40). At this point a problem arises. As it can be seen in Figure 1.2, if considering that $M(R)$ is mostly given by the luminous matter inside the galaxy (up to radius R), the velocity would fall as $v \sim R^{-1/2}$ (Keplerian rotation) at large radii. Indeed, this is not what data points show, since at large radii v remains approximately constant. This would bring to the conclusion that a higher quantity of mass should be present, under the form of some sort of dark halo in which the stellar disk is enclosed.

A similar reason is given by the analysis of galaxy clusters: the gravitational mass (inferred from the virial theorem) does not coincide with the luminous mass. Here again, some additional dark component would be needed (see e.g. [6]).
Another proof for dark matter is given by weak gravitational lensing observations (see e.g. [7]): the existence of this additional form of matter is observed and quantified by looking at angular distortions in the position of galaxies, and is consistent with other results coming from large scale structures.
A very strong proof of the existence of dark matter is given by observing the temperature anisotropies power spectrum of the Cosmic Microwave Background, which is extremely compatible with a ΛCDM scenario [2]. The absence of the dark matter would produce a totally different imprint. Any different model from this (such as MOND) is not able to reproduce the CMB angular power spectrum with such accuracy.
The non-existence of dark matter would also be correlated to difficulties for structure formation to take place (see e.g. [8]). During radiation dominated era, density perturbations would be washed out because of its interactions with it. On the other hand, the existence of dark matter, which does not interact with radiation, would allow to grow density perturbation when ordinary matter could not, providing the necessary potential

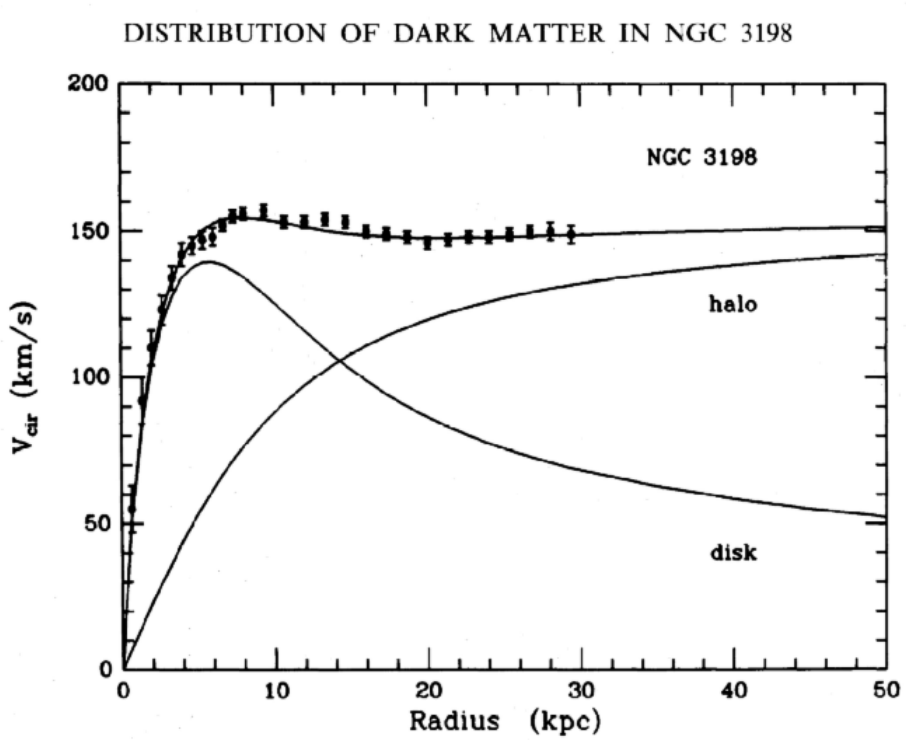

Figure 1.2: Rotation curve for the galaxy NGC 3198 [5]. It can be seen that, to justify the flat behavior at large radii, the existence of a dark matter halo is necessary, in addition to the ordinary matter disk.

wells for ordinary matter collapse.

When addressing the open issue of what dark matter may be composed of, the most popular picture regards the so called Weakly Interacting Massive Particles (WIMPs) [9]. WIMPs are hypotetical non-baryonic particles which are not part of the standard model of particle physics and would interact only slightly with ordinary matter. However, WIMPs have not been detected up to the present moment.
Another antecedent hypothesis to infer the nature of the dark matter concerns the so called MAssive Compact Halo Objects (MACHOs). With this term one can identify astronomical objects, such as black holes, brown dwarfs, white dwarfs, neutron stars and planets, which are characterized by a low luminosity/mass ratio (if compared to common stars). It is interesting to consider the hypothesis that there may be enough MACHOs to account for dark matter (or a significant fraction of it) under the form of Primordial Black Holes (PBHs). PBHs are thought to be produced at primordial times of the Universe because of collapse of overdense regions (deeper details about them are provided in Chapter 2). The idea that PBHs may constitute dark matter derives from the '90s (see e.g. [10, 11]) and were later obscured by some observational results and the advent of the "WIMPs as dark matter" model. However, actual constraints still leave the open possibility that PBHs in the mass range of $20M_\odot \lesssim M \lesssim 100M_\odot$ might exist in

abundance today (see Section 2.3) and the first detections of merging BHs binaries by GW experiments re-made this theory very popular [12].

1.2 Gravitational waves

Gravitational waves (GWs) are perturbations in the metric of the space-time which are produced by accelerated masses. They are transverse waves which move at the speed of light c.
Poincaré introduced this thematic in 1905, but they were analytically described by Einstein in General Relativity as wave solutions to the linearized field equations of gravity [1].
Starting from these equations and considering the weak gravitational field case, we can write the metric $g_{\mu\nu}$ in a point of the space-time in the form

$$g_{\mu\nu}(x) = \eta_{\mu\nu} + h_{\mu\nu}(x) \tag{1.41}$$

where $h_{\mu\nu}$ is a small perturbation of the Minkowski $\eta_{\mu\nu}$ ($|h_{\mu\nu}| \ll 1$). The fact that $h_{\mu\nu}$ is small allows us to to ignore contributes of order higher than one in this quantity, such that we are left with the linearized version of General Relativity.
When doing a gauge choice, we can set the so called Lorentz gauge condition in the form

$$\frac{\partial \bar{h}^{\mu\nu}}{\partial x^{\nu}} = 0 \tag{1.42}$$

where $\bar{h}^{\mu\nu} \equiv h_{\mu\nu} - \frac{1}{2}\eta_{\mu\nu}h$ and $h \equiv h^{\mu}_{\mu}$. A few mathematical calculations [13] can show that the linearization of the Einstein equation is

$$\Box \bar{h}^{\mu\nu} = -16\pi T_{\mu\nu}, \tag{1.43}$$

where $T_{\mu\nu}$ is the energy-momentum tensor (1.9) and $\Box$ is the d'Alambertian operator

$$\Box \equiv \eta^{\mu\nu}\partial_{\mu}\partial_{\nu} = -\frac{\partial^2}{\partial t^2} + \nabla^2. \tag{1.44}$$

Equation (1.43) shows that the components of $\bar{h}^{\mu\nu}$ obey a flat-space wave equation of the form

$$-\frac{\partial^2 f(x)}{\partial t^2} + \nabla^2 f(x) = j(x) \tag{1.45}$$

where $j(x)$ is the source. Solutions for this kind of problem are well known in physics.
The above expression (outside the source) reduces to

$$-\frac{\partial^2 f(x)}{\partial t^2} + \nabla^2 f(x) = 0 \tag{1.46}$$

if we consider $j(x)$ as a Dirac's delta (approximation we can do when far from the source).
Now, let's call (x, y, z) three orthogonal axes defining directions in space. Considering a

plane wave propagating on the z direction, we can write the perturbed metric tensor $h_{\mu\nu}$ as

$$h_{\mu\nu} = \begin{pmatrix} 0 & 0 & 0 & 0 \\ 0 & 1 & 0 & 0 \\ 0 & 0 & -1 & 0 \\ 0 & 0 & 0 & 0 \end{pmatrix} f(t-z) \tag{1.47}$$

where $f(t-z) = A\sin(\omega t + \phi)$ describes a plane wave propagating along z with amplitude A, pulsation ω and phase ϕ. With this recipe, we can write the metric element ds^2 as

$$ds^2 = -dt^2 + [1 + f(t-z)]dx^2 + [1 - f(t-z)]dy^2 + dz^2. \tag{1.48}$$

Now, let's suppose we have a circular distribution of test particles in the (x,y) plane. From Equation (1.48) we can define the following coordinate system (where we assume $\phi = 0$ for simplicity):

$$\begin{cases} X = x\left(1 + \frac{1}{2}A\sin(\omega t)\right) \\ Y = y\left(1 - \frac{1}{2}A\sin(\omega t)\right) \end{cases} \tag{1.49}$$

so that we can write the spatial metric element on the plane as

$$dS^2 = dX^2 + dY^2. \tag{1.50}$$

Since dX and dY in general are different while changing in time, the above Equation expresses an elliptical deformation: while time changes, we have a deformation along one axes and then along the other. The original circular shape is re-obtained for each multiple of the semi-period $T/2 = \pi/\omega$, for which $\frac{1}{2}Asin(\omega t) = -\frac{1}{2}Asin(\omega t)$. We have just described one independent polarization mode of gravitational waves.
The second polarization mode can be portrayed by rotating the axes of an angle $\phi = \pi/4$:

$$\begin{cases} x' = x\cos\phi + y\sin\phi \\ y' = -x\sin\phi + y\cos\phi \end{cases} \tag{1.51}$$

which gives

$$\begin{cases} x = \dfrac{1}{\sqrt{2}}(x' + y') \\ x = \dfrac{1}{\sqrt{2}}(x' - y') \end{cases} \tag{1.52}$$

The perturbed metric tensor for this polarization mode is

$$h^{\times}_{\mu\nu} = \begin{pmatrix} 0 & 0 & 0 & 0 \\ 0 & 0 & 1 & 0 \\ 0 & 1 & 0 & 0 \\ 0 & 0 & 0 & 0 \end{pmatrix} f_{\times}(t-z). \tag{1.53}$$

Renaming the metric element in Equation (1.47) (which describes only the first polarization mode) as $h_{\mu\nu}$ (and $f(t-z)$ as $f_+(t-z)$) we can write in a general way:

$$h_{\mu\nu} = h^{\times}_{\mu\nu} + h^{+}_{\mu\nu} = \begin{pmatrix} 0 & 0 & 0 & 0 \\ 0 & f_+ & f_\times & 0 \\ 0 & f_\times & -f_+ & 0 \\ 0 & 0 & 0 & 0 \end{pmatrix}. \tag{1.54}$$

In Figure 1.3 a schematic image of the effects of the two polarization modes of GWs is provided.

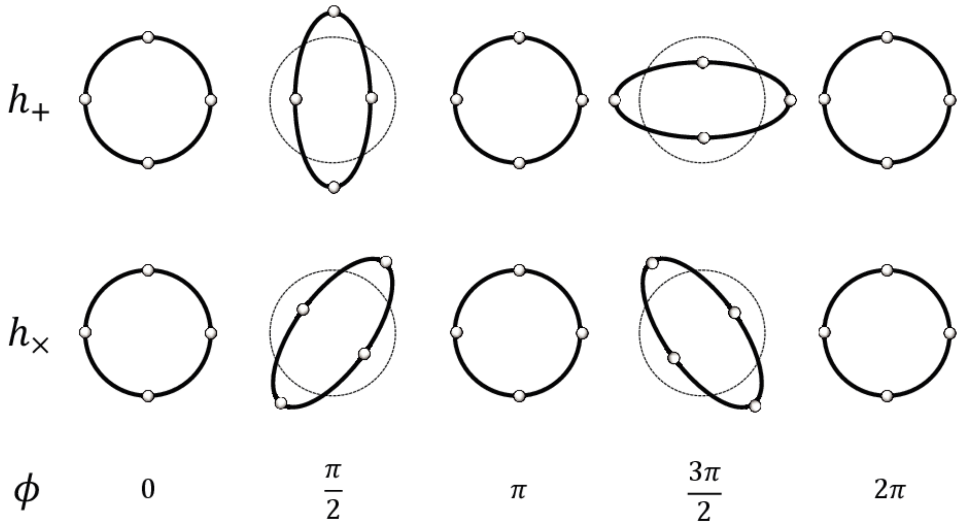

Figure 1.3: Effects on a circular distribution of test particles of the polarization modes h_+ and $h_\times$, respect to the phase ϕ.

Gravitational waves are produced when the $T^{\mu\nu}$ tensor changes in time in such a manner that it has a quadrupole or higher pole component. This is why for example a mass moving in an accelerated non-isotropic motion can generate GWs, while it would not be the same for a circular mass expanding or contracting in an isotropic way. Examples of objects/events that can generate GWs are:

- inspiraling and/or merging binary systems;
- non spherically symmetric Supernovae explosions;
- spinning neutron stars with deformities on surface;
- non symmetric inflationary expansion from the early Universe.

In this work our attention focused on the case of merging of BHs in binary systems.

1.2.1 Detection instruments

The leading method to detect GWs is based on the Michelson and Morley interferometer. This instrument permits to split light rays coming from a source into two beams, to finally collect both of them to a detector after they have traveled trough different paths along the two detector arms. At the detector the so called fringe pattern is visible: it is an effect caused by the sum of the two returning beams and depends on the different distance they traveled.
Now, consider a GW passing through an interferometer of this type while one laser beam is being split and then detected. Since GWs are transverse waves perturbing the space-time fabric, when one will pass through the detector, for example perpendicular to one of the two arms, one will contract, while the other will stretch. This induces a difference between the paths traveled by the two beams, consequently changing the interference fringe pattern. GWs are, basically, detected by observing changes in this pattern. They are effective even with different orientations, but the fringe pattern will depend on the orientation itself (since the interferometer arms will be stretched in different ways). Figure 1.4 provides a schematic portrait of the interferometer used for interferometers like the Laser Interferometer Gravitational Wave Observatory (LIGO).

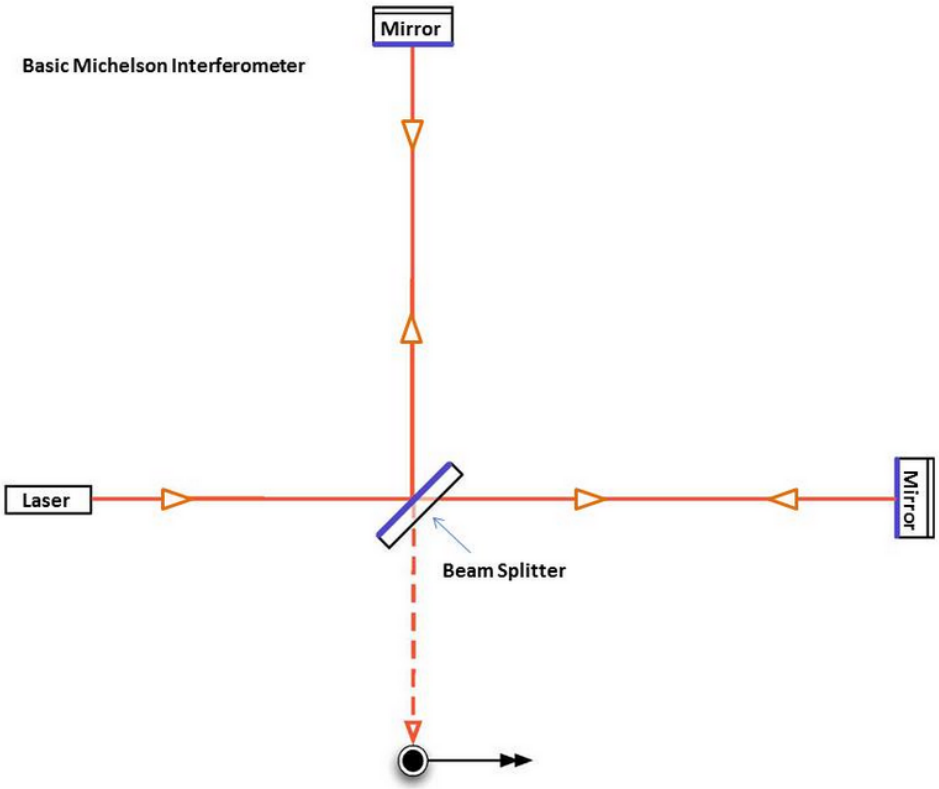

Figure 1.4: Schematic picture of the Michelson and Morley interferometer used for GW detectors like LIGO [14]. The laser is split into the two arms (between the beam splitter and the mirrors) and then recollected at the detector, where interference fringe patterns are analyzed.

LIGO [14] is the currently most sensitive GW experiment, composed by two ground based detectors, located in Livingston and Hanford (US), both of which have 4 km arms. In the most optimal conditions, a GW would change the length of the arms by a factor of roughly 10^{-18} m, which should be detected by the instrument. Then, Virgo [15] is a 3 km interferometer near Pisa (Italy) and the Japanese Kamioka Gravitational Wave Detector (KAGRA) [16] (3 km arms) and the LIGO India [17] (4 km arms) are being developed. In addition, improvements to both LIGO (advanced LIGO [18]) and Virgo are being developed to increase sensitivity. The Einstein Telescope [19] is still in the early design study phase, but it should be composed by three 10 km long underground arms forming a triangular shape, with two detectors.
Having multiple detectors in different sites is of fundamental importance for GW astronomy: firstly, it allows to better determine the source position and, secondly, it allows to identify and get rid of instrumental end environmental sources of noise.
Since for ground based detectors the noise contribution is strong, a huge advantage would be to consider space instruments, for which the noise contribution is extremely smaller. A space based observatory will also allow much longer arms, consequently increasing the instrument sensibility. This is what the Laser Interferometer Space Antenna (LISA) [20] aims to achieve, with a triangular shape of 2.5 million km arms. Planned launch date is 2034.

The LIGO experiment detected for the first time GWs coming from the coalescence event of a black hole binary system on September 14^{th} 2015, classified as GW150914 [21]. The colliding black holes had masses of $36^{+5}_{-4}M_{\odot}$ and $29^{+4}_{-4}M_{\odot}$, while the final black hole mass is $M_f = 62^{+4}_{-4}M_{\odot}$. It means that an energy amount of $3^{+0.5}_{-0.5}M_{\odot}c^2$ was radiated under the form of GWs. In Figures (1.5) and (1.6) some details about the detection of GW150914 are provided. As the reader can see, the observed strain amplitudes fit extremely well numerical relativity calculations outputs for a model with the parameters inferred for this event. In fact, the significance of the event was estimated to be greater than 5.1σ, corresponding to a false alarm rate smaller than one event per 203000 years.

1.2.2 Signal to Noise Ratio

The global output $s(t)$ of a GW detector can be written as a superposition of the noise $n(t)$ and a possible GW signal $h(t)$:

$$s(t) = n(t) + h(t). \tag{1.55}$$

The detectability of GWs passing through a detector depends on the so called Signal to Noise Ratio (SNR) ϱ, defined as [22]

$$\varrho^2 = \int_{f_{\min}}^{f_{\max}} df \frac{4|\hat{h}(f)|^2}{S_n(f)}, \tag{1.56}$$

where $f_{\min}$, $f_{\max}$ are the instrumental cut-off frequencies, f indicates the observed frequency, $\hat{h}(f)$ is the Fourier transform of the signal, defined according to the following

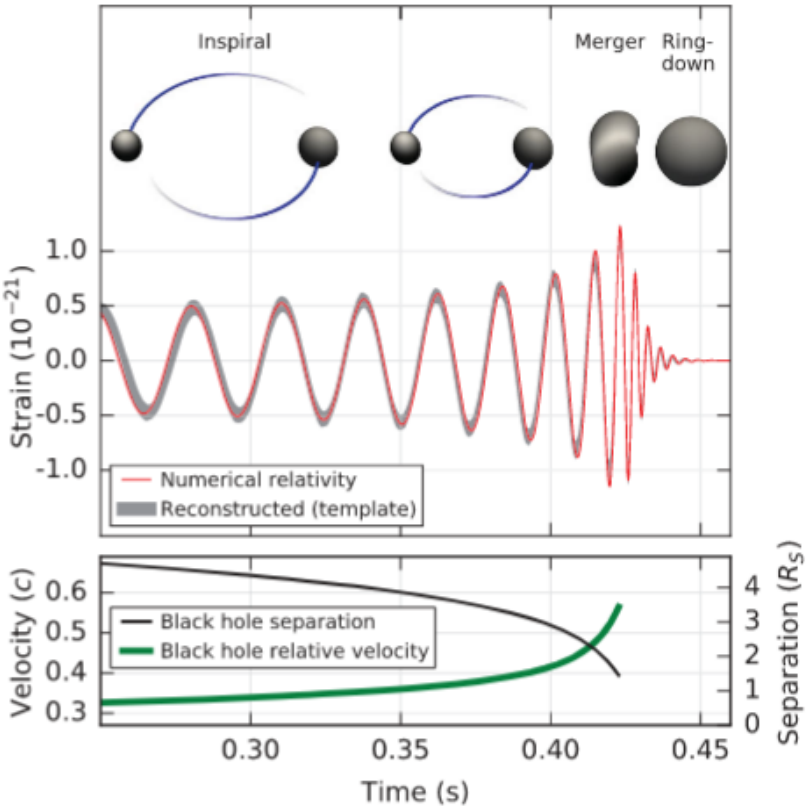

Figure 1.5: In the top side numerical relativity predictions of GW strain amplitude and reconstructed template (for the Hanford detector) are shown, for the three coalescence phases (inspiral, merger, ringdown). In the bottom side the black holes separation (in units of the Schwarzschild radius) and the effective relative velocity are provided [21].)

convention

$$\hat{h}(f) = \int_{-\infty}^{+\infty} dt\ h(t)e^{2\pi i f t}, \quad h(t) = \int_{-\infty}^{+\infty} df\ \hat{h}(f)e^{-2\pi i f t}, \tag{1.57}$$

and S_n is the so called one-sided noise power spectral density. Assuming that the noise is stationary and Gaussian, it can be expressed as

$$\langle \tilde{n}(f)\tilde{n}^*(f')\rangle = \frac{1}{2}\delta(f-f')S_n(f), \tag{1.58}$$

where the angle brackets have the meaning of an ensemble average over many noise realizations. If the noise is too hight compared to the signal, it is not possible do have a detection. Usually, a value of ϱ under which it is not possible to discern a signal is considered to be $\varrho \sim 8$ [23].
In the case of an inspiraling signal we can have a detection even if the instantaneous amplitude of the signal is below the noise level, since the signal is integrated over many orbits. In this case what it is used is the dimensionless characteristic strain

$$h_c^2(f) = 4f^2|\hat{h}(f)|^2 \tag{1.59}$$

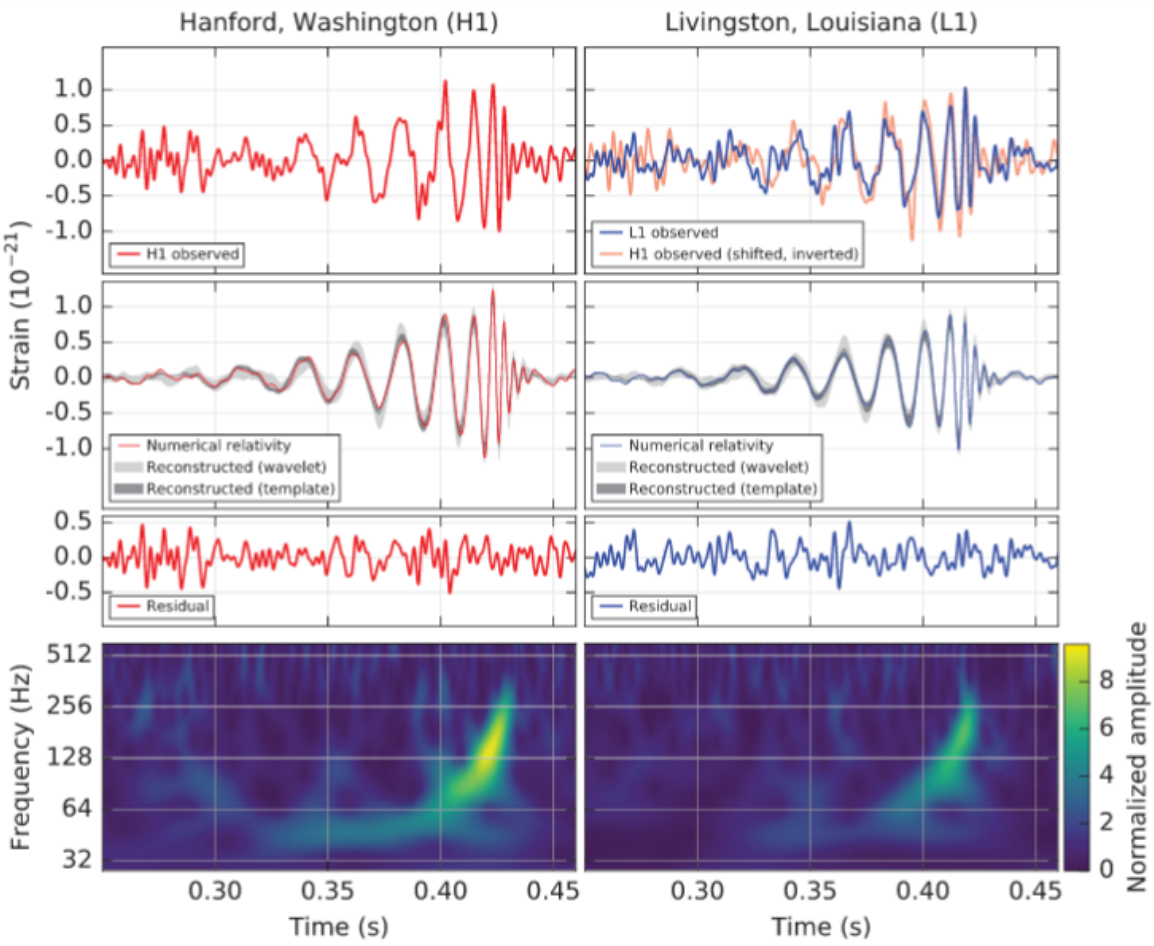

Figure 1.6: Detection of GW150914 by the LIGO Hanford (H1) and Livingston (L1) detectors. In the top row the observed GW strain amplitudes are provided. In the middle row the reconstructed waveforms are compared to the one predicted by numerical relativity calculations consistent with the system parameter attributed to GW150914 (and residuals). In the bottom row a time-frequency display of the strain data is provided. For specific details see [21].

and the SNR can be re-expressed as:

$$\varrho^2 = \int_{f_{\min}}^{f_{\max}} df \frac{h_c^2(f)}{f^2 S_n(f)}. \tag{1.60}$$

In reality the response of the detector does not depend only on the frequency of the gravitational wave, but also on the relative orientation with respect to the incoming wave, on the polarization of the wave and possibly on the orientation of the system. For this reason it is often used the orientation-averaged SNR (see e.g. [22, 24]):

$$\left\langle \varrho^2 \right\rangle = \frac{1}{5} \int_{f_{\min}}^{f_{\max}} df \frac{4|\hat{h}(f)|^2}{S_n(f)}. \tag{1.61}$$

The multiplicative factor actually slightly depends on the characteristics of the system considered, but it is usually near the value 1/5. In our analysis, we will consider this fixed

value for simplicity.

Chapter 2

Primordial Black Holes

Primordial Black Holes (PBHs) differ from standard stellar Black Holes because of their origin. They are hypothetical objects produced in the most common framework at early times, during radiation dominated era [25]. The authors of Refs. [26, 27, 28] were the first to show that, because of large density fluctuations in the primordial cosmic fluid, some extremely overdense regions may have overcome pressure forces and have collapsed to give birth to this kind of objects.
The specific process though which PBHs would be produced is still matter of discussion: many proposals have been made and some of them include, for example, collapse of cosmic string loops (see e.g. [29, 30, 31]), Bubble collisions (see e.g. [32, 33]), collapse of domain walls (see e.g. [34, 35, 36]) or large fluctuations produced during inflation (see e.g. [11, 37]).
Even if the proposed ways to form a PBH are multiple and very different from one to another, all of them rely on the same assumption: an overdense region (generated by some mechanism) in the primordial universe collapses gravitationally, giving birth to a black hole. We already know that BHs exist, since some stars at the end of their life cycle collapse in this kind of objects, so it makes sense to ask ourselves if BHs could really form at primordial times. Then, once we have multiple theories that would explain how these overdensities might form, we could ask ourselves how massive those PBHs would be, if they could have survived up to present time and if we can constrain their abundance today. The present knowledge about this issues is explained during this chapter. Just to anticipate it: PBHs forming because of collapse of large fluctuations have dimensions comparable to that of the horizon at formation time. They could exist still today in significant abundance in the mass range of $20M_\odot \lesssim M_{\rm PBH} \lesssim 100M_\odot$, where no robust constraints have been established. This opens another issue, already addressed in Section 1.1.5: PBHs might compose even a significant percentage of dark matter.
This hypothesis received a lot of attention from the scientific community especially after the GW experiments started detecting merging BHs binary systems. In fact, at this point it seems interesting to understand whether these merging black holes have primordial or stellar origins. As we will explain in Chapter 4, one possible way to discern the nature of these progenitors is by understanding what types of halos host them. Low mass halos have lower velocity dispersions, so that it would be easier for PBHs to gravitationally

bind when passing one near the other. On the other hand, in more massive halos PBHs would have higher velocities and it would be difficult for them to form a bound system. Then, if GWs were found to come from smaller halos, it would be very probable that their origin was the merger of two PBHs, also given the fact that lower mass halos are less luminous tracers. The quantity that enables us to distinguish between these two types of halos is given by the bias (4.1). Measuring this quantity for the GW events will indicate the nature of their host halos, letting us understand if the mergers we detect are actually from BHs of primordial origins.
Still, it is useful to stress that studying PBHs can have multiple useful impacts in the physics community, not just for the dark matter problem. As an example, studying them can lead to set constrains to primordial universe models. In addition, PBHs could be suitable candidates of seeds to super-massive black holes existing at the center of massive galaxies. Studying them can then open new doors and bring to potentially groundbreaking discoveries, even in the case they do not actually compose a significant portion of the dark matter.

2.1 Spherical Collapse

In this section some concepts about the PBHs formation process are provided, following the approach of the authors of Refs. [27, 28]. Only in this paragraph we will consider $G = c = 1$ for simplicity.
Consider a flat ($k = 0$) Friedmann-Robertson-Walker universe with a background energy density $\bar{\rho}$ and a spherical overdense region of physical radius R and homogeneous density $\rho = \bar{\rho}(1 + \delta)$, where δ expresses the magnitude of the overdensity. This overdense sphere, whose potential energy is given by

$$E_g \sim -\rho^2 R^5. \tag{2.1}$$

tends to collapse. Because of this process, its comoving radius decreases with time, while its physical radius firstly increases, but then decreases when the collapse overcomes cosmic expansion. Considering the maximum expansion time (at which the expansion kinetic energy is zero) one can say that in order to have a collapse it is necessary for gravitational energy to overcome pressure forces, which means that E_g has to be bigger than the internal energy $U \sim \rho R^3$, in other words

$$-E_g > U \quad \Longrightarrow \quad \rho R^2 \gtrsim 1, \tag{2.2}$$

which gives a lower limit to the dimension of a region that can undergo a collapse:

$$R \gtrsim \rho^{-1/2}. \tag{2.3}$$

It has also been stated that there is an upper limit to this dimension, beyond which the considered sphere would close up, forming a separate universe.

We can still consider a flat FRW metric. The interior of the collapsing homogeneous sphere can be described by a closed (k=1) FRW metric, which can be re-expressed as

$$ds^2 = -dt^2 + a(t)^2\left[d\chi^2 + sin^2\chi d\Omega^2\right] \tag{2.4}$$

if we consider the variable change $r = sin\chi$ (where $r \equiv R/a$ = comoving length). The coordinate χ is radial, comoving and dimensionless, while $L = a\chi$ is a physical length expressing the distance along a maximum circle between one point and a pole. Figure 2.1 shows a schematic comparison between r and χ.

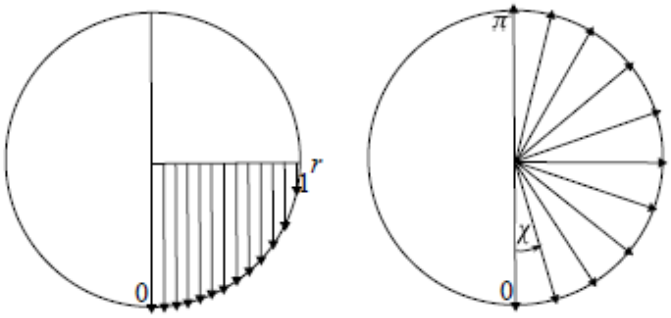

Figure 2.1: Coordinates r e χ as seen on a sphere section [38].

According to this definition, L increases monotonically from a lower value $L_l = 0$ (for $\chi = 0$) up to $L_m = \pi a_m$ (for $\chi = \pi$), while the physical radius of the sphere ($R = ar = a\sin\chi$) has a maximum value $R_m = a_m$ for $\chi = \pi/2$ and a minimum $R_l = 0$ for $\chi = \pi$.
In the interior of the sphere, the first Friedmann equation (1.11) with positive curvature at the maximum expansion instant, where $\dot{a} = 0$, yields

$$a_m = \sqrt{\frac{3}{8\pi\rho}} \sim \rho^{-1/2}, \tag{2.5}$$

therefore

$$L < L_m \sim \rho^{-1/2}. \tag{2.6}$$

Since the interior has positive curvature, we have that $R < L$, which leads to the existence of an upper limit to the sphere dimension, in fact

$$R < R_m < L_m \sim \rho^{-1/2}. \tag{2.7}$$

It has been argued [28] that beyond the limit R_m a separate universe would from. Even though this conclusion has been accepted for many years, recently it has been questioned [39, 38] and it has been shown that, even though the approximate estimation of the upper limit for a collapsing region formation is right, this limit arises from geometrical

consideration and not from a separate universe problem. In fact, the condition for the formation of a separate universe is $R \to 0$ instead of $R > R_{max}$ (Figure 2.2 can help visualize this situation). This result is very general, as it's based on purely geometrical matters. Despite this, the upper limit obtained is still considered valid and, combined with the lower limit found before, gives us a condition for the possible dimension that a region can have to collapse:

$$R \sim \rho^{-1/2} \sim t \tag{2.8}$$

which means that the unstable scale is of the order of the particle horizon at the collapse time t.
It's easy to show that the latter condition is also a limit for a PBHs dimension. In fact, from the necessary condition $R < R_S$ (where R_S is the Schwarzschild radius) one can infer that $R \lesssim M_{\mathrm{PBH}} \sim \rho R^3$, therefore $R \gtrsim \rho^{-1/2}$. Moreover, a given region would turn into a BH just right after the beginning of the collapse.
This result brings to another important consideration: the dimension of a forming BH (and consequently its mass M) depend heavily on its formation time. For example, a PBH formed at Planck time (before which General Relativity is not appropriate anymore, entering in the quantum gravity area) would have an initial mass of $10^{-5}g$ and a radius of $10^{-33}cm$ [25], while PBHs formed at later times would have higher masses.
In deeper detail, still under the assumption of spherical symmetry, it was shown (see e.g. [40, 41]) and confirmed by numerical works (see e.g. [42, 43, 44]) that M_{PBH} follows the critical scaling relation

$$M_{\mathrm{PBH}} = kM_H(\delta - \delta_c)^\gamma, \tag{2.9}$$

where M_H is the mass included inside the horizon at formation time, and the constants k, γ and δ_c are connected to the nature of the fluid which contains the overdensity δ at horizon-crossing [44].

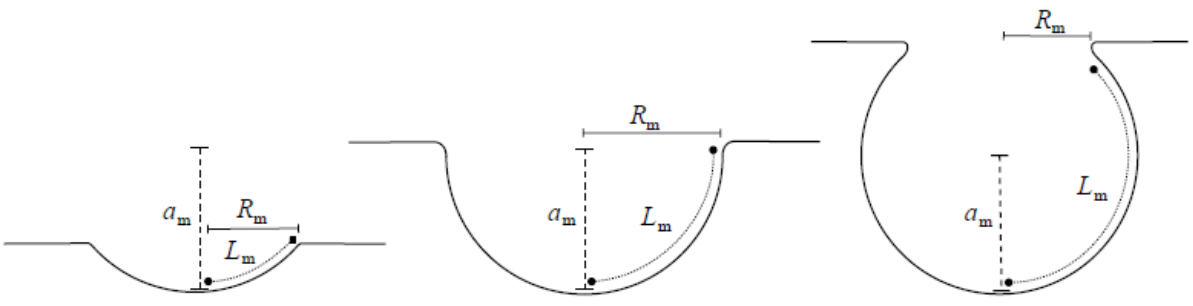

Figure 2.2: Sections of two over-dense regions in primordial universe. The suffixes m refer to the maximum expansion moment. It is intuitive to see that the separate universe condition is given by $R_m \to 0$ [38].

2.2 Primordial Black Holes evaporation

It is natural to wonder whether it is possible to see PBHs today or not. PBHs, as just said, can have masses at formation time from $10^{-5}g$ on, and it was also argued that they would not incur in a significant growth after their formation [28]. Anyway, there is a lower limit to PBHs masses that can still survive up to present time, in fact PBHs with masses up to $10^{15}g$ evaporate thanks to Hawking radiation in less than a Hubble time [45].
In fact, according to this theory, a BH emits as a black body with temperature T_{BH} given by

$$k_B T_{\mathrm{BH}} = \frac{\hbar g}{2\pi c} \tag{2.10}$$

where k_B is the Boltzmann constant, $\hbar$ is the reduced Planck constant and $g = GM_{\mathrm{PBH}}/R_s^2$ is the gravity acceleration at the Schwarzschild radius. In terms of the BH mass, equation (2.10) reads as

$$T_{\mathrm{BH}} = \frac{\hbar c^3}{8\pi G M_{\mathrm{PBH}} k} \simeq 6.4 \cdot 10^{-8} \left(\frac{M_{\mathrm{PBH}}}{M_\odot} \right)^{-1} \tag{2.11}$$

. The Hawking luminosity of a BH L_{BH} is given by the Stefan-Boltzmann law:

$$L_{\mathrm{BH}} = 4\pi R_s^2 \sigma T^4 \sim M_{\mathrm{PBH}}^2 M_{\mathrm{PBH}}^{-4} \sim M_{\mathrm{PBH}}^{-2}, \tag{2.12}$$

which tells us that for bigger masses the luminosity is smaller.
So, computing how much energy is lost for time interval we can write:

$$L_{BH} = \frac{dE}{dt} \Longrightarrow M_{\mathrm{PBH}}^{-2} \sim \frac{d}{dt}(M_{\mathrm{PBH}} c^2) \Longrightarrow dt \sim c^2 M_{\mathrm{PBH}}^2 dM \Longrightarrow t_{EV} \sim c^2 M_{\mathrm{PBH}}^3 \tag{2.13}$$

giving a first estimate of the evaporation time t_{EV}. With all the numerical factors taken into account, it's possible to get the result written before: PBHs with masses up to $10^{15}g$ would evaporate in a time smaller than the age of the universe. However, it's still a matter of discussion whether or not evaporation of this small mass BHs leaves Planck mass relics behind, as it was hypothesized that this evaporation process might stop when the PBHs reach the Planck mass [46].

2.3 Observational constraints

When considering more massive PBHs, which have not evaporated within a Hubble time, a substantial amount of constraints has been set using different methodologies. Many of them have excluded some mass ranges to see a significant quantity of PBHs today. These constraints (for a specific mass range) set a limit to the fraction $f_{\mathrm{PBH}} = \rho_{\mathrm{PBH}}/\rho_{\mathrm{DM}}$ of dark matter that can be composed by PBHs. Therefore, constraining PBHs abundance is a great way to tackle the dark matter problem explained in Section 1.1.5, as it leads to testing the hypothesis that PBHs could make at least part of this unknown component of the universe.

These constraints can be classified according to the specific effect associated with PBHs on which they are based. We can have dynamical, lensing, accretion and large scale structure constraints [47], which can be seen in Figure 2.3. Some of them, as will be explained, yield limits on the validity of the "Primordial black holes as dark matter" theory and are going to be explained in the following. They are: microlensing, halo wide binaries, Cosmic Microwave Background and ultra faint dwarf galaxies constraints.

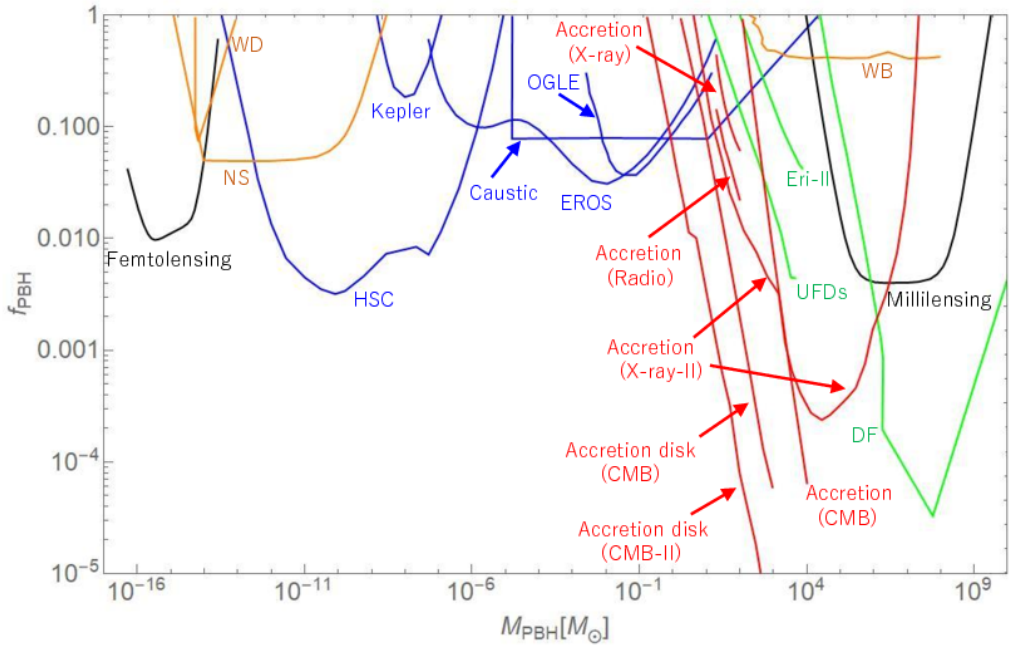

Figure 2.3: Constraints on the fraction $f_{\rm PBH}$ for different PBHs masses [47]. The colours refer to the effects associated with PBHs on which a specific constraint is based. more specifically: lensing constraints in blue [48, 49, 50, 51, 52], millilensing and femtolensing in black [53, 54], dynamical constraints based on disruptions of wide binaries, neutron stars and white dwarf in orange [55, 56, 57], dynamical friction and ultra faint dwarfs in green [58, 59]. Accretion in red [60, 61, 62, 63]. More details can be found in each reference.

2.3.1 $M_{\rm PBH} \lesssim 20M_\odot$: Microlensing constraints

According to General Relativity, light rays coming from a distant source are deflected because of the existence of a massive object (lens) between the source and the observer. This physical effect, called gravitational lensing, can make the observer see multiple images of the same source and induces also a distortion and a change in the observed image size, with a subsequent change in the number of photons being detected. The term microlensing is used if the lens is of stellar mass (or lighter).
Microlensing studies have excluded the possibility that PBHs of masses up to $\sim 20M_\odot$ could compose a significant fraction of dark matter today (see e.g. [64]). This constraint is

based on the following concept. Monitoring stars looking for microlensing effects caused by MACHOs in the Milky Way halo makes it possible to infer if dark matter is significantly made of this kind of objects. In this specific case, stars from the Large Magellanic Cloud were considered. As it is not possible to see a secondary image of the source star or an increase in its size, microlensing is measurable only through a flux amplification. The aim is to obtain values for the halo mass fraction $f_{\rm PBH}$ made of MACHOs, for different masses of the objects. Then, confronting the predicted number of events with the observations it's possible to rule out some mass ranges for MACHOs to be a significant component of the galactic halo.
At first, the MACHO project seemed to have revealed compact objects of $M_{\rm PBH} \sim 0.5 M_\odot$ contributing 20% of the halo mass [65]. These results were revisited and confuted at a later time [48] and the EROS project (which considered only bright stars, to achieve more accurate results) did not reveal any microlensing event, meaning that MACHOs between $0.6 \cdot 10^{-7} M_\odot \lesssim M_{\rm PBH} \lesssim 15\, M_\odot$ are ruled out as primary components of the galactic halo.

2.3.2 $M_{\rm PBH} \gtrsim 100 M_\odot$: Wide Binaries constraints

Wide halo binaries are binaries of stars with large separation (even the order of the parsec is possible) residing in the Galactic halo. These binaries are characterized by the fact that their orbital properties remain unchanged after formation time, except in case of interactions with perturbing masses. So, wide binaries can be used to establish the properties of their perturbers (and consequently understand their nature and define whether they are MACHOs or not). Monte Carlo simulations of evolution of this kind of binaries in presence of Machos can be made and compared to observations, giving the possibility to constrain MACHOs masses. Using this method, the authors of Ref. [66] obtained an upper limit for MACHOs masses of $\sim 45 M_\odot$, but it was later confuted [55], as it was strongly dependent on the inclusion of a spurious element in the considered observational sample, and the authors of Ref. [67] obtained an upper limit of approximately $100 M_\odot$, which is considered the most valid limit given by this constraint today.

2.3.3 $20 M_\odot \lesssim M_{\rm PBH} \lesssim 100 M_\odot$: Cosmic Microwave Background and Ultra Faint Dwarf Galaxies constraints

At this point, a mass window between the values of $\sim 20 - 100 M_\odot$ seems to allow the existence of a significant quantity of PBHs. Other attempts have been made to close this window, considering Cosmic Microwave Background and ultra-faint dwarf galaxies constraints.

CMB constraints

CMB constraints [68, 60] are based on the concept that accreting baryonic gas which is attracted by PBHs gravity can get ionized because of internal collisions between its particles or because of outgoing radiation. Such a high temperature is reached that an energy injection into the plasma happens, emanating X-rays outwards. The emitted radiation ionizes, excites or heats primordial gas, inducing distortions in the CMB power spectrum from the Planckian distribution and alterations in the decoupling time of CMB photons and the ionization history, consequently changing the power spectrum of the CMB temperature and polarization anisotropies. Not detecting this non-standard features in the CMB observables leads to constrain PBHs abundance.

Ultra Faint Dwarf Galaxies constraints

Ultra-faint dwarf galaxies have luminosities as low as approximately $1000 L_{\odot}$ and are thought to be dominated by dark matter. For what concerns this type of constraint, its concept can be exemplified by the case of Eridanus II [59], a galaxy that hosts a star cluster near its center. In a star cluster gravitational interactions lead to exchange of energy between components: two body interactions equalize the mean kinetic energy of different mass groups. If MACHOs are present, and are massive than stars, stars would gain energy from them and the cluster would expand. It is possible to derive MACHOs limits by requiring the timescales for dynamical heating to be larger than the cluster's age.

Both [68] and [59] would exclude the existence of an abundant quantity of PBHs of masses $20 - 100\ M_{\odot}$. More specifically, [68] rules masses over $0.1 M_{\odot}$ mass range, while [59] the the ones over $5 M_{\odot}$. Anyway, they have been rigorously questioned (see e.g. [69, 70, 71]) because based on a series of non-trivial caveats, leaving for the moment the possibility that a significant quantity of PBHs may exist still today within the mass range of approximately $20 - 100\ M_{\odot}$.

Chapter 3

Primordial black holes as dark matter

As expressed in the previous chapter, it is worth considering the possibility that PBHs of stellar masses could be constituent of the dark matter. This model is analyzed in detail in this Chapter.
Suppose we have two BHs of masses M_1 and M_2 in a galactic halo. When passing one near the other, they can become gravitationally bound and form a binary system if they lose enough energy under the form of GWs. The formation of a binary system is more probable to happen when the velocity of the components is not too high and their distance is short enough. We indicate with $M_t = M_1 + M_2$ the total and with $\mu = M_1 M_2/(M_1 + M_2)$ the reduced mass of the system. Once the two objects are gravitationally bound, they will start spiraling one around the other. In this way the system loses energy under the form of gravitational waves (GWs) which can be detected by present time instruments, such as LIGO-Virgo [72] (more details in Section 1.2). As a consequence, their orbital distance gradually decreases until they merge (deeper details on coalescence phases in Section 5.2.2).

We report in Table 3.1 information about the masses of all confirmed (by LIGO Scientific Collaboration and Virgo Collaboration) merging black holes binary systems detected up to present date [21, 73, 74, 75, 76]. There are only five of them, but it can be seen that many of the progenitors fall in the mass range of $20M_\odot \lesssim M_{1,2} \lesssim 40M_\odot$, which is compatible with the mass window in which PBHs could compose a significant fraction of dark matter today (as already expressed in Section 2.3).

3.1 Merger rate

The first merger of two black holes in a binary system (GW150914) detected by LIGO concerned objects of $\sim 30M_\odot$ each. After this breakthrough announcement, the "Primordial black holes as dark matter" theory (mentioned in section 1.1.5) gained a new strong interest as it was proposed that the just detected black holes could be of primordial

Table 3.1: Confirmed mergers of black holes binaries detected. We indicate $M_{1,2}$ the masses of the single components, while M_f is the final mass of the system, after the coalescence and z is the redshift of the system.

Event name	$M_1[M_\odot]$	$M_2[M_\odot]$	$M_f[M_\odot]$	z
GW150914 [21]	36^{+5}_{-4}	29^{+4}_{-4}	62^{+4}_{-4}	$0.09^{+0.03}_{-0.04}$
GW151226 [73]	$14.2^{+8.3}_{-3.7}$	$7.5^{+2.3}_{-2.3}$	$20.8^{+6.1}_{-1.7}$	$0.09^{+0.03}_{-0.04}$
GW170104 [74]	$31.2^{+8.4}_{-6.0}$	$19.4^{+5.3}_{-5.9}$	$50.7^{+5.9}_{-5.0}$	$0.18^{+0.08}_{-0.07}$
GW170608 [75]	12^{+7}_{-2}	7^{+2}_{-2}	$18.0^{+4.8}_{-0.9}$	$0.07^{+0.03}_{-0.03}$
GW170814 [76]	$30.5^{+5.7}_{-3.0}$	$25.3^{+2.8}_{-4.2}$	$50.3^{+3.2}_{-2.5}$	$0.11^{+0.03}_{-0.04}$

origin [12]. As a consequence, the hypothesis that BHs around this value of mass (which is coherent with most of the GW detections and consistent with the already mentioned $20M_\odot \lesssim M_{1,2} \lesssim 100M_\odot$ window for PBHs to exist in abundance today) could indeed be PBHs constituting a significant part of the dark matter was put forward, receiving a lot of attention from the scientific community.
This model aims to describe the possibility that, if the dark matter was made of $\sim 30M_\odot$ PBHs, binary systems would merge with a rate detectable by our experiments. We assume that that PBHs binary systems are formed inside galactic halos of masses M at different redshifts z. The rate of this binary formation, which is followed by a coalescence between the two bodies, is described by the total merger rate $\mathcal{R}_{\rm tot}(z)$. A fundamental way to verify if this model is worth being considered is to compare the estimate of $\mathcal{R}_{\rm tot}(z)$ that it yields to the one calculated after the detection of GW150914 by the LIGO team, who inferred a value of $2 - 53\, Gpc^{-3}yr^{-1}$ [77]. If these two values were not compatible, it would mean that this model could not be considered realistic.
Since we are considering BHs of equal mass, we will call $M_{\rm pbh} = M_1 = M_2$ the mass of the BHs in a binary system. If the halo had constant density $\rho_{\rm halo}$ the merger rate related to it would be

$$\mathcal{N} \approx \frac{1}{2} V \left(\frac{\rho_{\rm halo}}{M_{\rm pbh}} \right)^2 \sigma_{\rm PF} v_{\rm pbh} \tag{3.1}$$

where $\sigma_{\rm PF}$ is the cross-section for the formation of a binary (Pair Formation), $\rho_{\rm halo}/M_{\rm pbh}$ gives the BHs number density $n_{\rm pbh}$ and $n_{\rm pbh}\sigma_{\rm PF}v_{\rm pbh}$ is the merger rate for a specific BHs couple. Multiplying this factor for the number of BHs in the halo, given by $V(\rho/M_{\rm pbh})$, one can get the merger rate for the whole halo. The 1/2 factor appears not to count twice every merger.
Since in reality the halo density profile is more complex, the above expression for the encounters rate per halo (of mass M at redshift z) becomes:

$$\mathcal{R}(M,z) = 4\pi \int_0^{r_{\rm vir}} dr r^2 \frac{\rho^2_{\rm halo}(r)}{2M^2_{\rm pbh}} \langle \sigma_{\rm PF} v_{\rm pbh} \rangle \tag{3.2}$$

where angle brackets $\langle \cdot \rangle$ indicate an average over black holes relative velocity distribution $P(v_{\rm pbh})$ and M is the halo mass.
At this point, the total merger rate is computed convolving the merger rate per halo $\mathcal{R}(M,z)$ with the halo mass function $dn/dM(M,z)$:

$$\mathcal{R}_{\rm tot}(z) = \int dM \mathcal{R}(M,z) \frac{dn}{dM}(M,z). \tag{3.3}$$

3.2 Halo model

Describing galactic halos containing DM requires a specific density profile $\rho_{\rm halo}$. In the following we assume that dark matter halos have a Navarro-Frenk-White (NFW) profile [78]. It could be argued that this profile is unrealistic at the inner parts of the halo (since it asymptotically yields an infinite density value towards the center) and that choosing a different profile could significantly influence the outcome. Indeed, this is not the case: it was showed that results are insensitive to the chosen profile if its slope does not vary more rapidly than r^{-1} for $r \to 0$ [12]. The NFW profile reads as

$$\rho_{\rm NFW}(r) = \frac{\rho_s}{\frac{r}{r_s}\left(1+\frac{r}{r_s}\right)^2}, \tag{3.4}$$

where ρ_s and r_s are the characteristic density and radius. The characteristic radius is defined as the radius where

$$\left.\frac{d\log\rho(r)}{d\log r}\right|_{r_s} = -2. \tag{3.5}$$

The edge of the halo is designated by the virial radius $r_{\rm vir}$, inside which objects are virialized. The average density of a virialized object is approximately given by $\Delta_c \rho_c(z)$ [79], where $\rho_c(z) = \frac{3H^2(z)}{8\pi G}$ is the critical density and we set $\Delta_c = 200$, which is one of the most used values, also in agreement with numerical simulations [80]. Therefore the (virial) mass enclosed in such spherical region is given by

$$M_{\rm vir} = \frac{4\pi}{3} r^3_{\rm vir} \Delta_c \rho_c(z). \tag{3.6}$$

At the same time, the mass within a sphere of radius $r_{\rm vir}$ reads as

$$\begin{aligned} M(r_{\rm vir}) &= 4\pi \int_0^{r_{\rm vir}} dr r^2 \rho_{\rm NFW}(r) = 4\pi r_s^3 \rho_s \left[\log\frac{r_{\rm vir}+r_s}{r_s} - \frac{r_{\rm vir}}{r_{\rm vir}+r_s}\right] = \\ &= 4\pi r_s^3 \rho_s \left[\log(1+C) - \frac{C}{1+C}\right] = 4\pi r_s^3 \rho_s g(C), \end{aligned} \tag{3.7}$$

where we have defined the concentration parameter C as $r_{\rm vir} = Cr_s$, which indicates how much concentrate the halo is. From equations (3.6) and (3.7) we find that

$$\begin{aligned} r_s(M,z) &= \left(\frac{2GM}{\Delta_c H^2 C^3}\right)^{1/3}, \\ \rho_s(M,z) &= \frac{\Delta_c H^2 C^3}{8\pi G g(C)}. \end{aligned} \tag{3.8}$$

As can be seen in equation (3.3), in order to compute the total merger rate it is necessary to calculate

$$\begin{aligned} 4\pi \int_0^{r_{\rm vir}} dr\ r^2 \rho^2_{\rm NFW}(r) &= \frac{4\pi}{3} r_s^6 \rho_s^2 \left[\frac{1}{r_s^3} - \frac{1}{(r_{\rm vir}+r_s)^3}\right] = \frac{4\pi}{3} r_s^3 \rho_s^2 \left[1 - \frac{1}{(1+C)^3}\right] = \\ &= \frac{\Delta_c H^2 M}{24\pi G} \frac{C^3}{g^2(C)} \left[1 - \frac{1}{(1+C)^3}\right]. \end{aligned} \tag{3.9}$$

As can be noticed, the integral above can be expressed as a function of the concentration parameter C which, in general, is a function of both the halo mass and the redshift. To model its behavior we use the concentration-mass-redshift relations fit to dark matter N-body simulations [81, 82]. We follow [82] since it has a more extended halo mass function and redshift range: $10^{-7} \leq M/[h^{-1}M_\odot] \leq 10^{15}$ and $0 \leq z \leq 9$.It is important to notice that our choice in the specific concentration-mass relation does not affect our estimate of the merger rate: the authors of Ref. [12] have shown that considering another fit to N-body simulations ([81]) the final result is not influenced.
According to this reference the concentration parameter reads as

$$C(M,z) = c_0 \left(\frac{\nu}{\nu_0}\right)^{-\gamma_1} \left[1 + \left(\frac{\nu}{\nu_0}\right)^{1/\beta}\right]^{\beta(\gamma_1-\gamma_2)}, \tag{3.10}$$

where $\nu = \delta_{sc}/\sigma(M,z)$ is the so called dimensionless peak height, $\delta_{sc} = 1.686$ is the spherical collapse threshold and the redshift-dependent constants read as

$$\begin{aligned} c_0 &= 3.395(1+z)^{-0.215}, \\ \beta &= 0.307(1+z)^{0.540}, \\ \gamma_1 &= 0.628(1+z)^{-0.047}, \\ \gamma_2 &= 0.317(1+z)^{-0.893}, \\ \nu_0 &= \left[4.135 - 0.564(1+z) - 0.210(1+z)^2 + 0.0557(1+z)^3 - 0.00348(1+z)^4\right]/D(z), \end{aligned} \tag{3.11}$$

where the linear growth factor is given by

$$D(z) = \frac{\Omega_m(z)}{\Omega_m(0)} \frac{\Psi(0)}{\Psi(z)} (1+z)^{-1} \tag{3.12}$$

and

$$\Psi(z) = \Omega_m(z)^{4/7} - \Omega_\Lambda(z) + \left(1 + \frac{\Omega_m(z)}{2}\right)\left(1 + \frac{\Omega_\Lambda(z)}{70}\right),$$
$$\Omega_m(z) = \frac{\Omega_{m0}(1+z)^3}{\Omega_{\Lambda 0} + \Omega_{m0}(1+z)^3}, \tag{3.13}$$
$$\Omega_\Lambda(z) = 1 - \Omega_m(z) = \frac{\Omega_{\Lambda 0}}{\Omega_{\Lambda 0} + \Omega_{m0}(1+z)^3}.$$

The root mean squared density fluctuation can be approximated as

$$\sigma(M, z) = D(z)\frac{22.26\xi^{0.292}}{1 + 1.53\xi^{0.275} + 3.36\xi^{0.198}}, \tag{3.14}$$

where $\xi = \left(\frac{M}{10^{10}\ h^{-1}M_\odot}\right)^{-1}$.

3.3 Velocity distribution

Finally, let's turn our attention to calculate the velocity dispersion $v_{\rm dm}$ in the halo. By using the Virial Theorem, we can derive the circular velocity as a function of the radius

$$2E_k + E_g = 0 \quad \Longrightarrow \quad v_c^2(r) = \frac{GM(r)}{r}, \tag{3.15}$$

where E_k and E_g are the kinetic and the potential energies per particle respectively. It can be seen that $v_c(r)$ exhibits a maximum at $r_{\rm max} = c_{\rm max} r_s$, where $c_{\rm max} = 2.1626$. The virial velocity, i.e. the velocity at virial radius, reads as

$$v_{\rm vir} = v(r_{\rm vir}) = \sqrt{\frac{\Delta_c}{2}} HCr_s = \sqrt[6]{\frac{\Delta_c}{2}}(GMH)^{1/3}. \tag{3.16}$$

Finally we define $v_{\rm dm}$ as the escape velocity at radius $r_{\rm max}$, therefore, we have that

$$E_k + E_g = 0 \quad \Longrightarrow \quad v_{\rm dm}^2 = 2v_c^2(r_{\rm max}) = 2v_{\rm vir}^2 \frac{C}{C_{\rm max}} \frac{g(C_{\rm max})}{g(C)} = \frac{v_{\rm vir}^2}{R^2}, \tag{3.17}$$

where we included the C dependence in the function R. Matching N-body simulations [83], we approximate the relative velocity distribution within a halo as a Maxwell-Boltzmann distribution with a cut-off at the virial velocity $v_{\rm vir}$ i.e.,

$$P(v_{\rm pbh}, v_{\rm dm}, v_{\rm vir}) = e^{-v_{\rm pbh}^2/v_{\rm dm}^2} - e^{-v_{\rm vir}^2/v_{\rm dm}^2}. \tag{3.18}$$

3.4 Halo Mass Function

We chose the halo mass function calibrated on numerical simulations, but [12] showed that the classic analytic Press Schechter theory [84] yields basically the same output. Following Ref. [85], we model the halo mass function as

$$\frac{dn}{dM}(M, z) = f(\sigma)\frac{\Omega_m(z)\rho_c(z)}{M}\frac{d\log\sigma^{-1}}{dM}, \tag{3.19}$$

where

$$f(\sigma) = A\left[1 + \left(\frac{\sigma}{b}\right)^{-a}\right] e^{-k/\sigma^2}. \tag{3.20}$$

The parameters evolve in redshift as

$$\begin{aligned} A(z) &= A_0(1+z)^{-0.14}, \\ a(z) &= a_0(1+z)^{-0.06}, \\ b(z) &= b_0(1+z)^{-\alpha}, \\ \log_{10}\alpha &= -\left(\frac{0.75}{\log_{10}(\Delta_c/75)}\right)^{1.2}, \end{aligned} \tag{3.21}$$

where the constant parameters read as

$$A_0 = 0.186, \quad a_0 = 1.47, \quad b_0 = 2.57, \quad k = 1.19. \tag{3.22}$$

3.5 Cross section

Let's analyze in detail the black holes pair formation cross section $\sigma_{\rm PF}$. Note that it is practically equivalent to the merger cross section. In fact, the time between the binary system formation and the final merging has to be shorter than the Hubble time. This hypothesis is verified, as the merging time t_{mg} can be expressed as [86]

$$t_{mg} \approx \frac{3\sqrt{3}}{170\sqrt{85\pi}} \frac{(b v_{pbh})^{21/2}}{M_t^{19/2}\mu^{3/2}} \tag{3.23}$$

where b is the impact parameter. Depending on the values of the parameters, it can range from a few hours to the order of 10^3 years, but in any case it can be considered a very small time compared to a cosmological timescale. This condition also excludes the possibility that a binary system may be disrupted by the intrusion of a third body before the coalescence: the short merging time, combined with the small dimension of the binary system, makes this situation very unlikely.
Generally, the pair formation cross-section can be written as [87, 88]

$$\sigma_{\rm PF}(v_{\rm pbh}) = 2\pi\left(\frac{85\pi}{6\sqrt{2}}\right)^{2/7} \frac{G^2(M_1+M_2)^{10/7} M_1^{2/7} M_2^{2/7}}{c^{10/7} v_{\rm pbh}^{18/7}}. \tag{3.24}$$

For identical objects, like in our case, equation (3.24) reduces to

$$\sigma_{\rm PF}(v_{\rm pbh}) = \pi\left(\frac{85\pi}{3}\right)^{2/7} R_s^2 \left(\frac{c}{v_{\rm pbh}}\right)^{18/7} = 4\pi\left(\frac{85\pi}{3}\right)^{2/7} \frac{G^2 M_{\rm pbh}^2}{c^{10/7}} v_{\rm pbh}^{-18/7}, \tag{3.25}$$

where $R_s = 2GM_{\rm pbh}/c^2$ is the PBH Schwarzschild radius. The average over PBHs relative velocity distribution of the cross section times the velocity reads as

$$\begin{aligned}\langle\sigma_{\rm PF}(v_{\rm pbh})v_{\rm pbh}\rangle &= \int d^3v_{\rm pbh}\sigma_{\rm PF}(v_{\rm pbh})v_{\rm pbh}P(v_{\rm pbh},v_{\rm dm},v_{\rm vir}) = \\ &= 4\pi\left(\frac{85\pi}{3}\right)^{2/7}\frac{G^2M_{\rm pbh}^2}{c^{10/7}}\frac{\int_0^{v_{\rm vir}}dv_{\rm pbh}v_{\rm pbh}^{3/7}P(v_{\rm pbh},v_{\rm dm},v_{\rm vir})}{\int_0^{v_{\rm vir}}dv_{\rm pbh}v_{\rm pbh}^{2}P(v_{\rm pbh},v_{\rm dm},v_{\rm vir})} = \\ &= 4\pi\left(\frac{85\pi}{3}\right)^{2/7}\frac{G^2M_{\rm pbh}^2}{c^{10/7}}I(v_{\rm dm},v_{\rm vir}) = \\ &= \frac{24\pi}{5}\left(\frac{85\pi}{3}\right)^{2/7}\frac{G^2M_{\rm pbh}^2}{c^{10/7}v_{\rm dm}^{11/7}}I(R),\end{aligned} \tag{3.26}$$

where we used the variable $R(M,z)$ defined in equation (3.17) and we wrote the integral in equation (3.26) as

$$\begin{aligned}I(v_{\rm dm},v_{\rm vir}) &= \frac{6}{5}v_{\rm dm}^{-11/7}\frac{5\Gamma(5/7,0)^* - 7R^{10/7}e^{-R^2} - 5\Gamma(5/7,R^2)}{3\sqrt{\pi}{\rm Erf}[R]^\dagger - 6Re^{-R^2} - 4R^3e^{-R^2}} = \\ &= \frac{6}{5}v_{\rm dm}^{-11/7}I(R)\end{aligned} \tag{3.27}$$

The inspiraling dynamics is not the only way by two BHs could merge, since it could also happen after a direct collision. The cross section used to estimate the merger rate is referred to the general case, regardless of their trajectory, however LIGO would not be able to detect a direct collision between BHs: a spiraling behavior is needed to generate GWs detectable by the instruments. It means that a comparison between the LIGO estimate and the one from this theory would make sense only if the merger rate for direct merging would be negligible compared to the rest. This happens to be true, in fact it was verified that their fraction reaches only a maximum of $\sim 3\%$ for $v_{pbh} = 2000\ km\ s^{-1}$ [12]. Formation of binaries through non dissipative three body encounters is neglected too. In fact, even though the rate of this binary formation is non-negligible in smaller halos, the system formed is usually so wide that it does not merge within a Hubble time [87, 89] Then, this mechanism does not influence LIGO observations.
We shall clarify a possible question that may arise. Since the described model considers PBHs all of the same mass, it could be natural to think what would happen if considering PBHs of different masses. In Figure 3.1 we show how a change in the two masses M_1 and M_2 could affect the estimate of the pair- formation cross section (3.24). As the reader can see, the impact of considering masses between 20 and 40 $M_\odot$ (interval of values reflecting confirmed detections by LIGO) is quite low, meaning that our methodology would still be valid if a mass spread around $30M_\odot$ was present.

*Incomplete Gamma function: $\Gamma(a,z) = \int_z^\infty dt\ t^{a-1}e^{-t}$.

†Error function: ${\rm Erf}[x] = \frac{2}{\sqrt{\pi}}\int_0^x dt\ e^{-t^2}$.

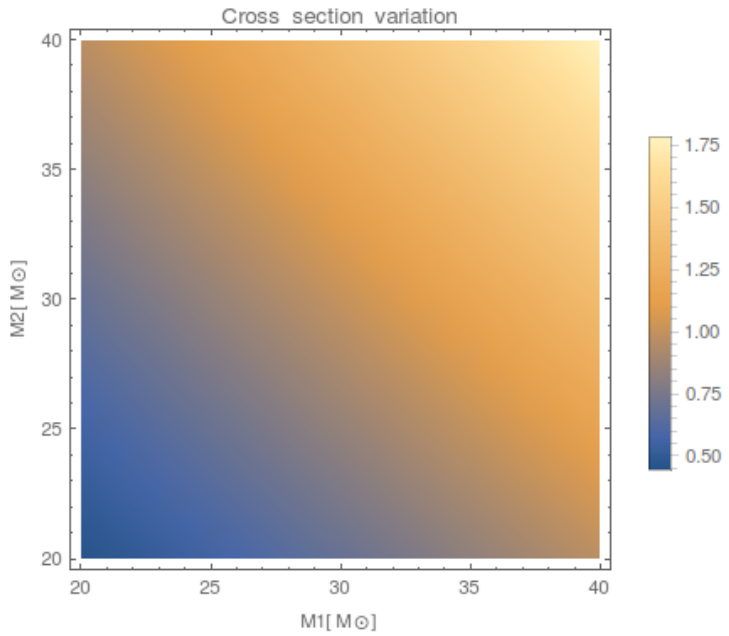

Figure 3.1: This plot shows the pair formation cross section (3.24) normalized to the value of $\sigma_{\rm PF}(30M_\odot, 30M_\odot)$. It can be seen that, for different values of the PBHs masses, this fraction doesn't deviate significantly from unity.

3.6 Merger rate results

By using equations (3.9) and (3.26) along with equation (3.2) we find that the merger rate per halo of mass M is expressed as

$$\mathcal{R}(M,z) = \frac{2^{11/42}}{10}\left(\frac{85\pi}{3}\right)^{2/7}\frac{G^{10/21}\Delta_c^{31/42}H^{31/21}}{c^{10/7}}\frac{M^{10/21}C^3}{g^2(C)}\left(1-\frac{1}{(1+C)^3}\right)R^{11/7}I(R), \tag{3.28}$$

where we corrected few typos in Equation 8 of Ref. [12].
Now we can compute the total merger rate from Equation (3.3), taking particular care in choosing the upper and lower limits. The former does not influence significantly the integration result because of the exponential falloff of dn/dM. We chose to integrate up to $10^{15}h^{-1}M_\odot$. On the other hand, the latter has higher influence on the outcome.
Following the work of [12], we neglected all halos with shorter evaporation timescale (i.e. all halos lighter than $400M_\odot$). Small halos tend to evaporate because of periodic ejection of objects by dynamical relaxation processes, with a timescale t_e given by [90]

$$t_e \approx (14N/\ln(N))[r_{vir}/(Cv_{dm})] \tag{3.29}$$

where N in the number of single BHs in the halo. If the halo mass is $M = 400M_\odot$, the resulting timescale is approximately $\sim 3Gyr$. While during matter dominated era the evaporation process is compensated by accretion of new material and mergers between smaller halos, this process slows down at dark energy domination, at redshift $z \lesssim 0.3$, which corresponds to $3\,Gyr$ ago. For this reasons, we set the lower limit of the integral to $400M_\odot$.

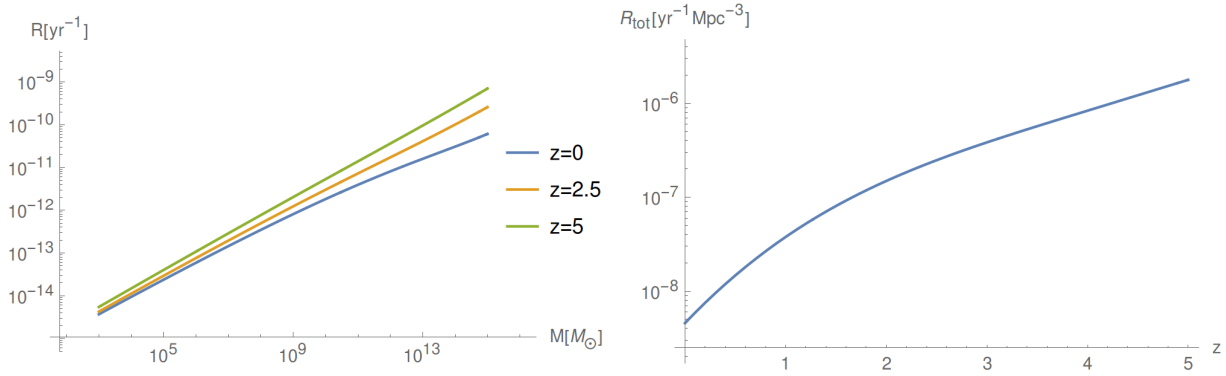

Figure 3.2: *Left*: merger rate per halo $\mathcal{R}(M, z)$ predicted by the "30 $M_\odot$ PBHs as dark matter" model, in function of the halo mass M. Different redshift values z are provided. *Right*: total merger rate $\mathcal{R}_{tot}(z)$ predicted by the same model, in function of the redshift z.

In Figure 3.3 the contribution of halos of different masses to the merger rate is provided. It is possible to see that the contribution is almost exclusively given by small mass halos (up to $\sim 10^6 M_\odot$). This is a very important result which will be at the basis of this work, as will be explained in Chapter 4.

In Figure 3.2 we provide the behavior of the merger rate per halo $\mathcal{R}(M, z)$ in function of the halo mass for different redshifts. As expected, more massive halos dominate the merger rate, as more PBHs can merge (since $M_{\rm PBH}$ is fixed). Instead, in Figure 3.2 it is shown how $\mathcal{R}_{tot}(z)$ varies with redshift. Increasing z, $\mathcal{R}_{tot}(z)$ grows too. In fact, plotting the halo mass function (for fixed halo mass M) it can be seen that it is an increasing function with z, as $\mathcal{R}(M, z)$. Integrating the product of the two will necessary give a monotonically increasing function.
Considering higher redshift sources can be very useful: since the total merger rate is higher, a bigger amount of sources coming from those redshifts can be detected, and it will be a great advantage in the galaxies - GWs cross-correlation process that will be explicated in Chapter 4.

Finally, we can confront our estimate (evaluated at $z = 0$) with the one made by LIGO [77] (which is a mean up to redshift 0.09). The LIGO estimate is

$$\mathcal{R}_{tot}^{\rm LIGO} = 2 - 53\ Gpc^{-3} yr^{-1} \tag{3.30}$$

while we estimate a value of

$$\mathcal{R}_{tot}(z = 0) \sim 4\ Gpc^{-3} yr^{-1} \tag{3.31}$$

We note that, given all the assumptions and the complexity of the model, we just aimed to give an order of magnitude estimate, not an exact value. On the other hand, also the prediction by the LIGO team is very flexible, given the very small amount of data

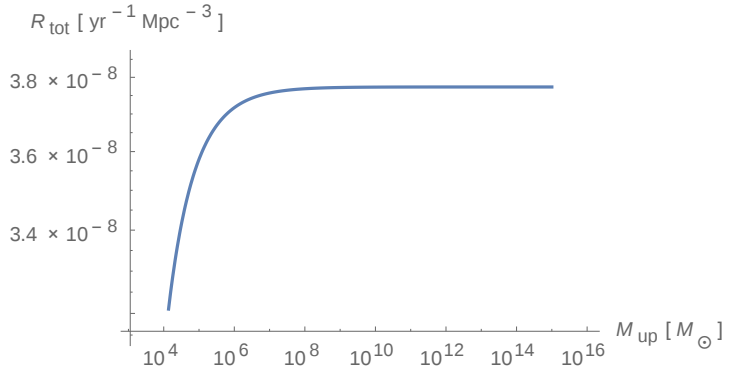

Figure 3.3: The value of the total merger rate $\mathcal{R}_{tot}$ obtained considering only halos of masses up to a limit M_{up} is provided. The plot shows the case at redshift $z = 1$. As the reader can see, smaller halos give the most contribution to the merger rate, since after the value of $M_{up} \sim 10^6 M_\odot$ the integral of Equation 3.3 yields basically the same result.

available. It can be seen that the two values are consistent. This is a very important result, since it means that it is worthwhile to consider this theory and, on the basis of the studies conduced up to now, it still makes sense to consider the hypothesis that BHs observed by LIGO might be of primordial origin and that PBHs of $\sim 30 M_\odot$ might constitute dark matter.

Chapter 4

Galaxies - Gravitational Waves Cross-Correlation

After having described in the previous Chapter the "$30M_{\odot}$ PBHs as dark matter" theory, it is of fundamental importance to find methods that could verify or falsify it. In this case, the way to test it would be given by the possibility to understand if the merging BHs detected trough GW experiments are of stellar or primordial origin. A method that would permit to infer the origins of BHs mergers progenitors is based on cross-correlating GW events with galaxy maps.
As shown in Figure 3.3 mergers between PBHs would occur mostly in low-mass halos. In fact, in more massive halos the mean velocity is higher than the one in less heavy halos (see e.g. Equation (3.15) and [91]). As a consequence, it is much more probable that two PBHs could form a binary system in low mass halos since they would need to lose less energy under GWs to become gravitationally bounded. Having higher velocities would make it more difficult to happen.
Moreover, lighter halos are also the less luminous [92], since they do not have enough mass to produce a large amount of stars. Then, once a significant amount of GWs coming from BHs mergers will be detected, it will be useful to correlate the corresponding events map with a mapping of galaxies. If GWs are found to come mostly from heavy halos, which means that they would be highly correlated with luminous galaxies, it would prove that the BHs progenitors would be of stellar origin. On the other hand, if GWs were poorly correlated with galaxies (i.e. if they are mostly detected from low mass halos) it would mean that these progenitors are more probable to have primordial origin.

4.1 Bias

According to the current standard cosmological framework, galaxies form by condensation of gas falling into extended dark matter structures' potential wells. Even though it is intuitive to think that galaxies distribution traces that of dark matter, the correlation between the two is not straightforward, in fact galaxy distribution does not exactly mirror

the underlying dark matter one. There is a non-trivial relation between tracers and matter, known with the name of bias.
To describe this mismatch, the concept of bias was introduced for the first time by Kaiser [93] and was further developed by Bardeen and others [94]. They assumed that baryons might have condensed more efficiently in correspondence of rare, high-density peaks of the matter density field, obtaining the following mathematical expression for the linear bias b_g at a given time and position x:

$$\delta_g(x) \equiv \frac{n_g(x) - \bar{n}_g}{\bar{n}_g} = b_g \delta(x) \tag{4.1}$$

where $\delta(x)$ and $\delta_g(x)$ are the local contrast of matter and of a specific tracer (e.g. galaxies or clusters of galaxies) respectively, while $\bar{n}_g(x)$ and n_g are the mean comoving density of the tracer and its local value respectively. This is a simplified equation that holds when $\delta \ll 1$. As a consequence, we can relate the two-point correlation function $\xi_g(r)$ of the given tracer to the matter correlation function $\xi(r)$ related in the following way:

$$\xi_g(r) \simeq b_g^2 \xi(r). \tag{4.2}$$

Not all dark matter halos have the same bias. In particular, we can roughly divide them into low mass and high mass halos.

- *Low mass halos.* The bias for this type of halos has already been estimated analytically [95] and it reads as:

  $$b_h = 1 + \frac{\nu^2 - 1}{\delta_{sc}} \tag{4.3}$$

  where ν and δ_{sc} are defined in Section 3.2. The authors of Ref. [96] calculated that for halo masses of $M < 10^6 M_\odot$ (which include the vast majority of halos which would host PBHs merge events, as seen in Figure 3.3), its value does not deviate significantly from $b_h \sim 0.5$.

- *High mass halos.* This type of halos typically host a huge amount of star forming galaxies that can be used as luminous tracers. For this type of objects, the bias assumes approximately the value of $b_g \sim 1.4$.

At this point it is evident that the bias is a quantity that can be used to distinguish between primordial and stellar BHs. Once a rich set of GW detections will be available, it will be possible to determine how much they correlate with luminous star forming galaxies, and the bias associated to GW events will express it. Depending on whether $b_{\rm GW}$ will be closer to b_h or b_g, BHs progenitors will be more plausible to be of primordial or stellar origin, or a mixture of the two.

4.1.1 Magnification bias

The magnification bias for galaxies expresses the fact that cosmic magnification (which is the lensing effect that low redshift structures have on more distant objects) changes the

relative number of sources detected at a given redshift and fixed magnitude limit. Two opposite effects derive from it, so that a distribution of galaxies can appear more or less numerous. On the one hand, gravitational lensing magnifies fluxes of sources, so that some galaxies right under the magnitude detection limit can actually be seen, increasing the number of detected sources. On the other hand, lensing causes magnification of the image size too. This means that the sources which are near the border of the observed sky area might fall outside it because of size magnification, and not be detected anymore. Depending on which of these two effects dominates, we can have an increase or a decrease in the sources number.
The magnification bias is defined as [97, 98]

$$s(z) = -\frac{2}{5}\left.\frac{d\log_{10} N_g(z, L > L_{\rm lim})}{d\log_{10} L}\right|_{L_{\rm lim}} = \left.\frac{d\log_{10} N_g(z, L > L_{\rm lim})}{dm}\right|_{m_{\rm lim}}, \tag{4.4}$$

where N_g is the (cumulative) galaxy number density per redshift and per steradian with luminosity above $L_{\rm lim}$, while m is the apparent magnitude of the sources. Note that sometimes in literature magnification bias is also indicated as $\mathcal{Q} = 5s(z)/2$.
The above expression is related to the case were the observed sources are galaxies, but in Section 5.2.2 we showed how we extrapolated this concepts for the case of GWs, obtaining a specific expression for the magnification bias of this kind of sources.

4.1.2 Evolution bias

This quantity accounts for the source counts evolution. New galaxies form over time and it is necessary to take it into account to have more realistic results. The evolution bias is given by:

$$f_{\rm evo}(z) = \frac{1}{aH}\frac{d}{d\tau}\ln\left(a^3\frac{d\bar{N}(z, L > L_{\rm lim})}{dz d\Omega}\right), \tag{4.5}$$

where τ is the conformal time and $d\bar{N}(z, L > L_{\rm lim})/dz/d\Omega$ indicates the true number density of galaxies per redshift and per solid angle in the Universe above a certain luminosity limit $L_{\rm lim}$. It can be estimated from the luminosity function [99], but given the uncertainties in modeling galaxy evolution, for simplicity we assume that the observed $dN(z)/dz/d\Omega$ still gives a good approximation of $f_{\rm evo}(z)$. This is an approximation often used (see e.g. [100]) and is justified by the fact that $f_{\rm evo}(z)$ appears only in subleading terms, so that uncertainties in its modeling do not significantly affect the final result.

4.2 Galaxies number counts

We now address the problem of how determine a realistic estimate of the number counts of galaxy sources.
When looking at galaxies in the sky, we observe them on our background light cone. We can determine their direction $\mathbf{n}$ and their redshift z and for each value of these two parameters it is possible to define the observed galaxy number counts. The observed

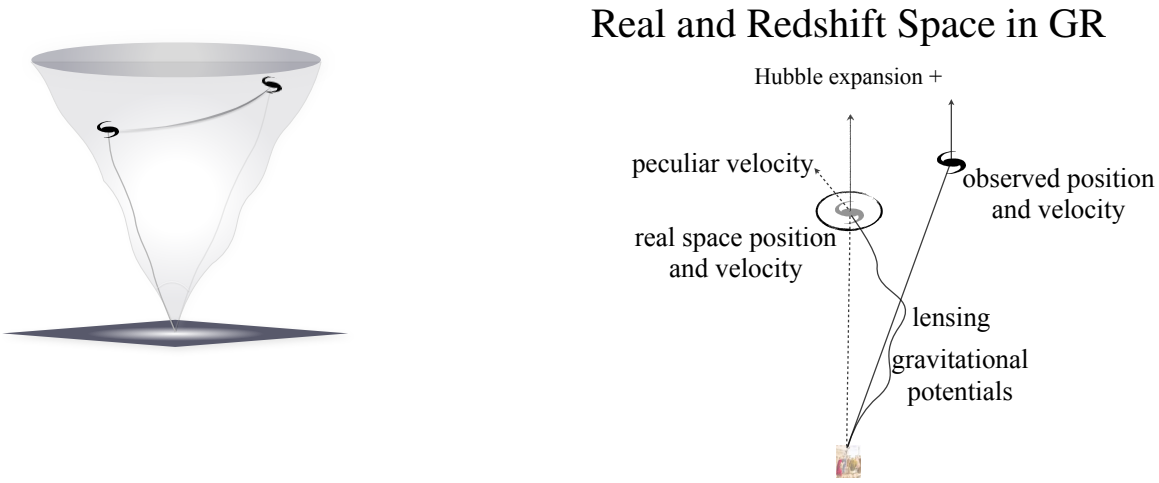

Figure 4.1: *Left*: we observe positions and redshifts of galaxies in our perturbed past light cone. *Right*: schematic effects on the apparent position of a galaxy by the peculiar velocity, gravitational potential and lensing terms. We observe the galaxy in a different position than the real one [101].

overdensity can be named $\Delta_{obs}(\mathbf{n}, z)$. This quantity is an observable and, therefore, is gauge-invariant. It is what we called $\delta_g(x)$ in Equation (4.1).
It is interesting to take into account all possible relativistic effects, in addition to the classical Newtonian ones. Developing them in linear perturbation theory, $\Delta_{obs}(\mathbf{n}, z)$ can be written as the sum of different contributions:

$$\Delta_{\rm obs}(\mathbf{n}, z) = \Delta_\delta(\mathbf{n}, z) + \Delta_{\rm rsd}(\mathbf{n}, z) + \Delta_{\rm v}(\mathbf{n}, z) + \Delta_\kappa(\mathbf{n}, z) + \Delta_{\rm pot}(\mathbf{n}, z). \tag{4.6}$$

Figure 4.1 provides a schematic idea of how these effect influence observations. The meaning of each one component of Equation (4.6) will be briefly explained in the following. All the not integrated quantities are evaluated at conformal time $\tau(z)$ and at position $r(z)\mathbf{n} = (\tau_0 - \tau(z))\mathbf{n}$. Here $r(z)$ is the conformal distance on the light cone, $r(z) = \tau_0 - \tau(z)$. A prime indicates a derivative w.r.t. conformal time. $\mathcal{H}(z) = aH(z)$ is the so called conformal Hubble parameter.

- $\Delta_\delta(\mathbf{n}, z)$. This is just given by the galaxy density field. Following Equation (4.1), this is given by

  $$\Delta_\delta(\mathbf{n}, z) = b(z, k)\ \delta_{\rm co}\left(r(z)\mathbf{n}, \tau(z)\right) \tag{4.7}$$

  where $\delta_{\rm co}$ is the matter density contrast in the comoving gauge and $b(z, k)$ is the bias given in Equation (4.1).

- $\Delta_{\rm rsd}(\mathbf{n}, z)$. This quantity is given by

  $$\Delta_{\rm rsd}(\mathbf{n}, z) = \frac{1}{\mathcal{H}(z)}\partial_r(\mathbf{V}\cdot\mathbf{n}) \tag{4.8}$$

where **V** is the peculiar velocity. This term arises from the existence of peculiar motions which affect our measurements of the redshift (i.e. our estimates of radial distances). This means that the distribution of sources in the redshift space is distorted respect to the one in the real space. In Figure the two-dimensional correlation function in redshift space is provided, as a function of the radial π and transverse σ separations.

One of the firsts to study this subject was Kaiser [103], who pointed out that when

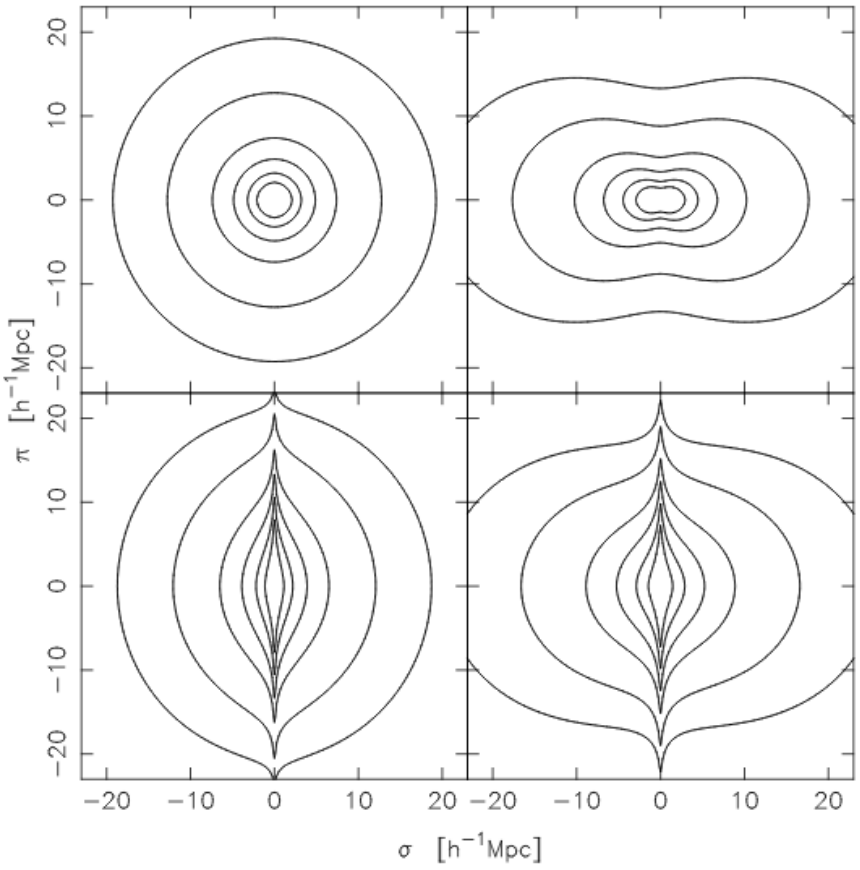

Figure 4.2: Example of how the two point correlation function $\xi(\sigma, \pi)$ - as a function of the radial separation along the line of sight π and the transverse separation on the sky σ - can change its shape in the redshift space due to the "fingers of God" and the Kaiser effect [102]. Solid lines portray different values of $\xi(\sigma, \pi)$ for different models. *Top left*: undistorted correlation function. *Top right*: squeeze due to the Kaiser effect due to coherent infall. *Bottom left*: elongation due to the "fingers of God" caused by random motions. *Bottom right*: result of the sum of both the two effects.

galaxies undergo a coherent infall towards a specific point, an effect of flattening of the correlation function is induced. This effect is typical of large (linear) scales.
On the other hand, if we consider galaxies with random velocity dispersions in groups or clusters at small (non-linear scales) we also have distortions in the redshifts space. In this case, since this affects only the redshift and not the position on the sky, the

distortion is a radial stretch, effect commonly known as "fingers of God" [104].

- $\Delta_{\rm v}(\mathbf{n}, z)$. This term expresses all other possible peculiar velocities effects, influencing the measured redshift of the sources. It is written as

$$\Delta_{\rm v}(\mathbf{n}, z) = \left[\frac{\mathcal{H}'}{\mathcal{H}^2} + \frac{2-5s(z)}{r\mathcal{H}} + 5s(z) - f_{\rm evo}(z)\right](\mathbf{V}\cdot\mathbf{n}) + \left[3\mathcal{H} - f_{\rm evo}(z)\right]\Delta^{-1}(\nabla\cdot\mathbf{V}) \tag{4.9}$$

  where $s(z)$ and $f_{evo}(z)$ are the magnification and the evolution bias that were described in Sections 4.1.1 and 4.1.2.

- $\Delta_{\kappa}(\mathbf{n}, z)$. This term derives from relativistic corrections and provides the contribution of gravitational lensing. It can be written as

$$\Delta_{\kappa}(\mathbf{n}, z) = (2-5s(z))\kappa = -\frac{(2-5s(z))}{2}\int_0^{r(z)} dr\frac{r(z)-r}{r(z)r}\Delta_2(\Phi+\Psi) \tag{4.10}$$

  where Φ and Ψ are the Bardeen potentials. Gravitational lensing causes an apparent modification to the angular position of the sources, significantly altering their number counts. It is related to the magnification bias effects that were illustrated before.

- $\Delta_{\rm pot}(\mathbf{n}, z)$. This is the gravitational potential term and derives from relativistic corrections too. It can be expressed as

$$\begin{aligned}\Delta_{\rm pot}(\mathbf{n}, z) = {} & (5s(z)-2)\Phi + \Psi + \mathcal{H}^{-1}\Phi' \\ & + \left[\frac{\mathcal{H}'}{\mathcal{H}^2} + \frac{2-5s}{r\mathcal{H}} + 5s(z) - f_{\rm evo}(z)\right]\cdot\left[\Psi + \int_0^{r(z)} dr(\Phi'+\Psi')\right] \\ & + \frac{2-5s}{r(z)}\int_0^{r(z)} dr(\Phi+\Psi).\end{aligned} \tag{4.11}$$

  This term causes an apparent alteration in the radial position of the sources. It contains terms such as Sachs-Wolf effects and the Shapiro time-delay. The first one causes a shift in photons energy when they cross potential wells between the source and the observer. In fact, when falling inside a well they lose energy, but if in the meantime the system originating this well evolves (changing its profundity) the photons will not lose the same amount of energy they gained while falling, consequently getting out with redshifted or blueshifted. The Shapiro time-delay, instead, is connected to the space dilatation around massive object, which makes the photons travel for a longer path between source and observer, respect to the case of absence of masses.

4.3 Cross-correlation power spectrum

To quantify the correlation between our two tracers, we can use measurements of their number counts. Following approach of [96], based on the theoretical framework from

[105, 106], cross-correlation between two observables (in our case g and GW) can be described by the cross-correlation power spectrum C_l^{gGW}, defined as

$$\langle a_{lm}^{\mathrm{g}} a_{l'm'}^{\mathrm{GW}*} \rangle \equiv C_l^{\mathrm{gGW}} \delta_{ll'} \delta_{mm'}. \tag{4.12}$$

A few mathematical calculations give [107]

$$C_l^{\mathrm{gGW}}(z_1, z_2) = r \int \frac{4\pi dk}{k} \mathcal{P}(k) \Delta_l^{\mathrm{g}}(z_1, k) \Delta_l^{\mathrm{GW}}(z_2, k), \tag{4.13}$$

where r is the so called cross-correlation coefficient ($r = 1$ in the case of auto-correlation) and $\mathcal{P}(k)$ is the matter power spectrum (1.34). The $\Delta_l(z_i, k)$ are referred to an infinitesimal redshift interval around the value z_i. In the case of a more realistic redshift bin, they are substituted by

$$\Delta_l^i(k) = \int dz \frac{dN}{dz} W_i(z) \Delta_l(z_i, k) \tag{4.14}$$

where $W_i(z)$ are the so called window functions (usually taken as gaussian) and dN/dz is the redshift galaxy distribution. This integral is normalized to unity within the redshift interval of the bin. Note that the index i refers to the redshift bin considered. The full expression for $\Delta_l(z, k)$ is obtained by expanding in spherical armonics the expressions for Δ_{obs} (see e.g. [101] for details).
The errors in the auto and cross-correlations are given by [108]

$$\begin{aligned}
\sigma_{C_l^{\mathrm{gGW}}} &= \sqrt{\frac{\left(C_l^{\mathrm{gGW}}\right)^2 + \left[\left(C_l^{\mathrm{gg}} + \frac{1}{N_{\mathrm{g}}}\right)\left(C_l^{\mathrm{GWGW}} + \frac{1}{N_{\mathrm{GW}}}\right)\right]}{(2l+1) f_{sky}}}, \\
\sigma_{C_l^{\mathrm{gg}}} &= \sqrt{\frac{2\left[C_l^{\mathrm{gg}} + \frac{1}{N_{\mathrm{g}}}\right]^2}{(2l+1) f_{sky}}}, \\
\sigma_{C_l^{\mathrm{GWGW}}} &= \sqrt{\frac{2\left[C_l^{\mathrm{GWGW}} + \frac{1}{N_{\mathrm{GW}}}\right]^2}{(2l+1) f_{sky}}},
\end{aligned} \tag{4.15}$$

where f_{sky} is the observed fraction of the sky and $N_{\mathrm{g,GW}}$ is the mean number of detected sources per steradiant, which can be obtained computing the integral of $\frac{dN_{\mathrm{g,GW}}}{dz}$ over the interested redshifts. The specific redshift distribution considered for our two tracer are going to be provided in Chapter 5.

4.4 Fisher analysis

In this section we describe the basis of the Fisher matrix formalism [109], tool we used to determine if future surveys will be able to infer the origins of the progenitors of merging black-holes binaries thanks to the technique of cross-correlation between galaxies and GWs.
The Fisher matrix approach is a tool often used to forecast how well a future experiment can perform, in terms of how big the uncertainties in the parameters that will be measured would be. The great advantage of this technique is that it is definitely quick if compared to another way to obtain the same results: developing simulations of the observables to subsequently estimate the parameters, as one would do with the actual data. The use of simulations would give a more robust forecast, but it is not always easy to set in practice and can take enormous amounts of time. The Fisher matrix approach, instead, can provide a quick but still valid result, before doing the experiment and without even simulating it.
Suppose we have a set of data. In our case they are the C_l, but for other types of experiments they could be, for example, the temperature of the CMB in different pixels of the sky. Our data set depends on a series of parameters θ_i that can be measured by the given experiment. We now introduce the likelihood function $\mathcal{L}$. It expresses what is the probability of measuring some data, given an underlying theory that is described by some parameters. If $\mathcal{L}$ is a narrow function it means that, given the data, only a few values of those parameters would be able to produce the measured output. On the other hand, if $\mathcal{L}$ is a wide function, the parameters of the theory can vary much, still producing the same measurable data. Modeling the likelihood with a Gaussian curve, the Fisher matrix element $\alpha - \beta$ is defined as

$$F_{\alpha\beta} = -\left\langle \frac{\partial^2 \ln \mathcal{L}}{\partial\theta_\alpha \partial\theta_\beta} \right\rangle \tag{4.16}$$

and it can be shown [109] that $F_{\alpha\beta}$ (expressing our data as the C_l) can be re-written as

$$F_{\alpha\beta} = \sum_l \frac{\partial C_l}{\partial\theta_\alpha} \frac{\partial C_l}{\partial\theta_\beta} \sigma_{C_l}^{-2} \tag{4.17}$$

where l expresses the multipole order and the σ_{C_l} are given by Equation (4.15).
Given the Fisher matrix, if we want to estimate with which precision a given parameter θ_i will be determined, we just need to evaluate the following quantity:

$$\varsigma_{\theta_i} = \sqrt{(F^{-1})_{\theta_i\theta_i}} \tag{4.18}$$

where $(F^{-1})_{\alpha\beta}$ is the element $\alpha - \beta$ of the inverted of the Fisher matrix. Here, describing the parameters distribution with a Gaussian, ς_{θ_i} is the 1-sigma uncertainty on θ_i.
Globally speaking, the bigger the Fisher matrix elements will be, the better the parameters will be constrained. It can also be understood in an intuitive way: if the two derivative terms in Equation (4.17) are big, it means that the measured C_l change significantly if the parameters change: then, it would be less difficult to estimate those parameters since we can measure very different C_l even just for small changes in the various θ_i. Also, it

is obvious that if the errors associated to the measured C_l are smaller, the constraining power of the given survey will be higher.

Specific details of our work will be given in Chapter 5, but it is worth stressing from now why the Fisher matrix approach was useful for this work. As already said, PBHs and stellar BHs are usually found in different types of halos. As a consequence, they belong to regions characterized by a different value of the bias (as said in Section 4.1). Developing a Fisher analysis considering the bias of the GW sources as one of the parameters to constrain enables us to determine how well this quantity can be measured with future surveys. If it will be measured well enough (i.e. if the error $\varsigma_{b_{\rm GW}}$ associated to it is small enough) we will be able to infer the nature of the progenitors of merging BHs binary systems detected through GW experiments.

Chapter 5

Methodology

In Chapter 4 the theoretical concepts at the base of this work were described. In this Chapter we are going to provide the specific assumptions made, the tools used to develop this project and the obtained results.

5.1 Use of the CLASS code

The most fundamental tool for this project was the Cosmic Linear Anisotropy Solving System (CLASS) [110]. This is a Boltzmann code often used in Cosmology, written in the C language and characterized by good flexibility, accuracy and speed. The CLASS code can simulate the evolution of linear perturbations in the universe and compute CMB and large scale structure observables.
We made use of CLASS to compute the angular projections C_l from Equation (4.13), which give the cross-correlation power spectra between our two tracers: galaxies and GW events. The basic version of CLASS does not allow correlations between different tracers. For this reason, we modified the code so that it could compute separately the functions $\Delta_l^{\mathrm{g},\mathrm{GW},i}(k)$ and then combine them together to compute the C_l^{gGW}:

$$C_l^{\mathrm{gGW}}(z_1, z_2) = r \int \frac{4\pi dk}{k} \mathcal{P}(k) \Delta_l^{\mathrm{g}}(z_1, k) \Delta_l^{\mathrm{GW}}(z_2, k), \tag{5.1}$$

where

$$\begin{aligned} \Delta_l^{g,i}(k) &= \int dz \frac{dN_{\mathrm{g}}}{dz} W_i(z) \Delta_l(z_i, k), \\ \Delta_l^{GW,i}(k) &= \int dz \frac{dN_{\mathrm{GW}}}{dz} W_i(z) \Delta_l(z_i, k). \end{aligned} \tag{5.2}$$

All the quantities above were defined in Equations from (4.12) to (4.14). The modified code we obtained now allows to compute cross-correlations between two different tracer populations that the user can choose. Another characteristic of CLASS is that it allows the user to choose which contribution to the observed number counts $\Delta_{obs}(\mathbf{n}, z)$ (4.6) must be taken into account. Table 5.1 shows how these contributions are divided and how they

Table 5.1: As explained in Section 4.2, the observed number count of a given tracer is subject to different types of corrections, both relativistic and non. CLASS lets the user choose which to take into account during computations, just specifying their call keys among the inputs.

Call Key	Contribution to Δ_{obs}
density	Δ_δ
rsd	$\Delta_{rsd} + \Delta_v$
lensing	Δ_κ
gr	Δ_{pot}

can be included into the computation.

We chose to repeat our analysis in three different cases, considering the following contributions:

- Case I: density+rsd;
- Case II: density+rsd+lensing;
- Case III: density+rsd+lensing+gr.

Finally, CLASS gives the possibility to compute both auto and cross-correlations in different redshift bins. The redshift range that can be taken into analysis depends on the survey considered. In our case we chose to consider the following redshift range:

$$1 \leq z \leq 4, \tag{5.3}$$

which has been divided into 3 bins of same width:

$$1 \leq z_{\mathrm{bin}_1} \leq 2 \quad ; \quad 2 \leq z_{\mathrm{bin}_2} \leq 3 \quad ; \quad 3 \leq z_{\mathrm{bin}_3} \leq 4. \tag{5.4}$$

The next Section will provide in detail the characteristic of tracers with the assumptions made to describe them.

5.2 Multi-tracing

We already wrote that this work is based on cross-correlating galaxies with GW events, but it is now necessary to explain better what our two tracers actually are. We also said that the way to discern between BHs of stellar and primordial origin is to measure the bias of the hosting galaxies (which gives an indication of the nature of BHs). Our first tracer is given by star forming galaxies (details in Section 5.2.1), which have a bias b_{g}. If BHs progenitors had stellar origins, they would come preferentially from this type of

galaxies (we have already explained in Chapter 4 why) and they would have obviously the same bias $b_{\rm GW}^{\rm stellar} = b_{\rm g}$. Our second tracer is given by GWs, but this is not enough to characterize it. We assume, in fact, that our GWs will come from PBHs mergers (i.e. from low mass halos), and then are characterized by a bias value $b_{\rm GW}^{\rm primordial} = b_h$. For simplicity, in the following we will write b_{GW} instead of $b_{\rm GW}^{\rm primordial}$, and we will just talk about GWs, without specifying every time that we actually intend GWs supposed to come from low mass halos.

5.2.1 First tracer: Star Forming Galaxies

Star forming galaxies compose our first tracer. As already mentioned, they typically live in more massive halos, where the mean velocities are higher. PBHs binary formation would be very difficult to have place: for this reason, merging BHs binary systems from this regions are more likely to have stellar origins.
Our sample was taken from Ref. [111]. The star forming galaxies we considered are a group of radio sources described in the simulations of Ref. [112] for a survey with detection threshold $10\,\mu Jy$. These sources can be detected at redshifts even higher than those of our chosen window $1 \leq z \leq 4$. In the following more details about some physical quantities characterizing this tracer are provided.

Bias

The prescription for the galaxy bias (introduced in Section 4.1) comes from the simulations of [112]. It was also used in other works dealing with the same type of sources (see e.g. [113]). In Figure 5.1 the plot for this quantity in function of the redshift z is provided, while its analytic formula reads as

$$b_{\rm g}(z) = \begin{cases} a_1\, e^{a_2 z} & z < 3 \\ b_g(3) & z \geq 3 \end{cases} \tag{5.5}$$

where $a_1 = 0.755$ and $a_2 = 0.368$. The redshift cutoff at $z = 3$ was imposed by the authors of Ref. [112] because of simulation reasons. In fact, their approach was to consider a fixed halo mass for each population, but the validity of this assumption breaks down at higher z where the bias $b_{\rm g}(z)$ would exponentially blow-up. For this reason, the bias was held constant after a given cut-off, to avoid unrealistic results.
Equation (5.5) was implemented in the CLASS input file. As the reader can see, this value does not deviate much from $b_{\rm g}(z) \sim 1.4$, which explains the affirmation made in Section 4.1.

Magnification bias

When having to select the most appropriate magnification bias $s(z)$ (introduced in Section 4.1.1) for this tracer we considered once again the work of Ref. [112]. In this case no well defined outcomes were available (not only in this Reference, but in all scientific literature). Anyway, the result can be extrapolated from one of the plots of this reference, which

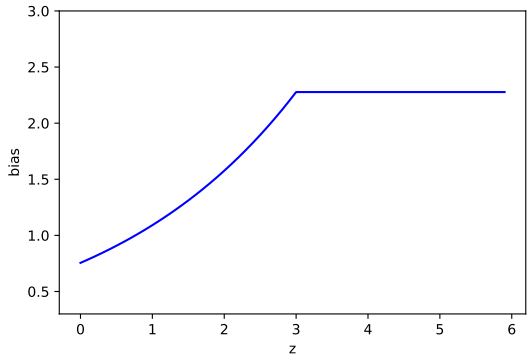

Figure 5.1: Behavior for the star forming galaxies bias. It can be seen that in the redshift range $1 \leq z \leq 4$ the mean value is ~ 1.4.

led us to consider a constant value of $s(z) = 0$. In fact, they showed that the slope of the source number counts function assumes values close to 0, which leads to our choice through the definition of magnification bias (4.4).

Redshift distribution

The redshift distribution $dN_{\rm g}/dz$ is of great importance, since it is necessary to compute the window function $W_l^{\rm g}(k)$ which determine the various C_l. In addition to this, it also plays a role in the expression of the evolution bias f_{evo} defined in Equation (4.5) and in the errors related to the C_l (4.15).
The authors of Ref. [111] provide a table with the expected number density of detectable elements of our tracer. Interpolating this data, we obtain the following expression:

$$\frac{dN_{\rm g}}{dz d\Omega} = b_1 \, z^{b_2} \, e^{-b_3 z} \tag{5.6}$$

with $b_1 = 2.085 \cdot 10^7$, $b_2 = 1.049$ and $b_3 = 1.337$. Note that Equation (4.14) requires that this function must be normalized to unity in the redshift window considered, but CLASS takes care of doing so. On the other end, when computing the total number of galaxies $n_{\rm g}$ for the errors σ_{C_l} in Equations (4.15), the right multiplicative factor is fundamental. In this case, we had to switch from deg^{-2} to $steradiant^{-2}$. Our $dN_{\rm g}/dz$ (obtained integrating Equation (5.6) over the full sky) and the cumulative number of sources $N_{g\,\rm tot}$, given by integrating it, are plotted in Figure 5.2 in function of the redshift.

5.2.2 Second tracer: Gravitational Waves

Our second tracer is given by GW events. Since this tracer is not commonly used as galaxies, it required more modeling work.

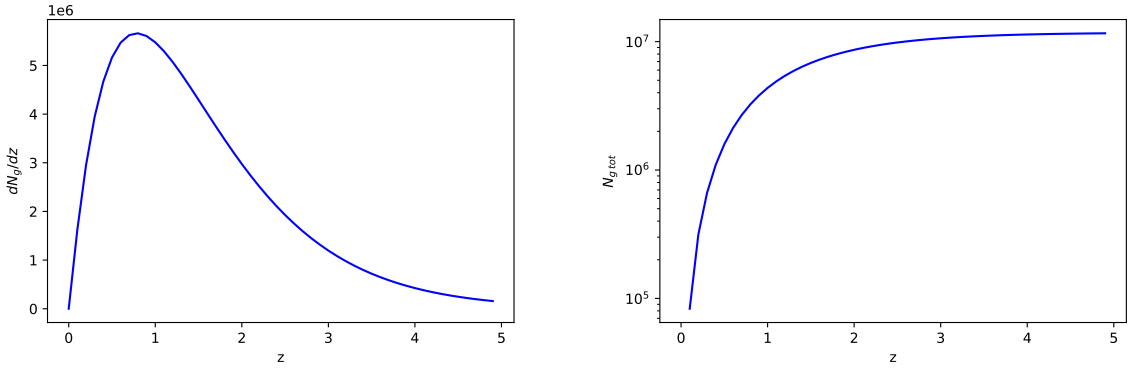

Figure 5.2: *Left*: Redshift distribution $dN_{\rm g}/dz$ for our sample of star forming galaxies. *Right*: Cumulative number of star forming galaxies sources $N_{g\,\rm tot}$. It is the result of the integral of the redshift distribution from $z = 0$ up to a redshift z.

Detector

Since GW astronomy is a very flourish area of work, and since GW experiments are subject to multiple upgrades that will let us detect GW events with more efficiency, we chose as a second tracer the events that would be detected by a futuristic instrument, whose characteristics are shown in the following.
The reason why we needed to consider a hypothetical future instrument is given by the fact that, as we will explain in Chapter 6, today instruments such as aLIGO would not be able to accomplish the task we require to test the "primordial black holes as dark matter" theory.
We considered a configuration of the Advanced LIGO instrument [18], which is characterized by a one-sided noise power spectral density $S_n(f)$ that can be analytically approximated with the expression provided by the author of Ref. [114], that reads as

$$S_n(f) = A^2 \left[c_{-4} f^{-4} + c_0 + c_{3/4} f^{3/4} + c_{3/2} f^{3/2} + c_{9/4} f^{9/4}\right], \tag{5.7}$$

where the constants are given by

$$\begin{aligned} A &= 10^{-24}, \\ c_{-4} &= 5.5124 \cdot 10^{7}, \\ c_0 &= 17.7622, \\ c_{3/4} &= -0.1050, \\ c_{3/2} &= 7.2709 \cdot 10^{-4}, \\ c_{9/4} &= 1.231 \cdot 10^{-6}. \end{aligned} \tag{5.8}$$

Anyway, this configuration would reach the SNR threshold $\varrho_{\rm lim} = 8$ below a redshift value of 2 (depending on the orientation of the system) for mergers of approximately $30 M_\odot$ BHs. Since we want to forecast the results that could be obtained with future improved

instruments, in our analysis we changed the amplitude A of $S_n(f)$ to the value

$$A' = 1.5 \cdot 10^{-25}, \tag{5.9}$$

corresponding to an instrument that would reach the $\varrho_{\rm lim} = 8$ threshold at approximately redshift 5 (for the case of orientation-averaged SNR (1.61)). A comparison between the aLIGO $S_n(f)$ and ours is provided in Figure 5.3.

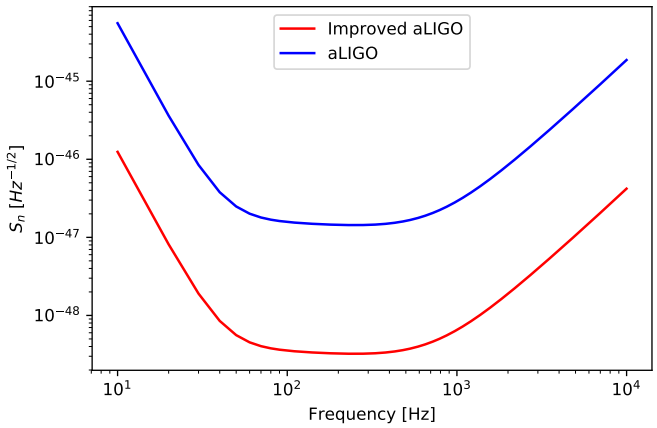

Figure 5.3: Comparison between the noise power spectral density of aLIGO (which has an amplitude $A = 10^{24}$) and our hypothetical futuristic experiment ($A' = 1.5 \cdot 10^{-25}$). It is evident that in our S_n is lower, yielding a higher SNR.

Note that, at this point, our chosen redshift window of analysis $1 \leq z \leq 4$ is justified, since both of our tracers would be detectable in this range.

Coalescence signal

The coalescence process between two BHs can be schematically divided in three subsequent stages (inspiral, merger, ringdown), characterized by the emission of GWs in different frequency ranges [24]:

- *Inspiral.* This is a phase in which the orbit is not dynamically unstable yet, since it is higher than the so called innermost stable circular orbit (ISCO) of radius $R_{ISCO} \sim 6GM/c^2$, which defines the smallest stable orbit possible.
  The frequency (at the source) determining the end of this phase and the beginning of the next one is

$$f_{\rm merger} = f_m = 4100 \left(\frac{M_t}{M_\odot}\right)^{-1} \text{ Hz}. \tag{5.10}$$

The spectral energy density at the source of the GWs during this phase, if we use the circular orbit approximation, is given by

$$\left.\frac{dE}{df_s}\right|_{\text{inspiral}} = \frac{1}{3}\pi^{2/3}\mu M_t^{2/3} G^{2/3} c^{-3} f_s^{-1/3}, \tag{5.11}$$

where $f_s = (1+z)f$ is the gravitational wave frequency at source and f is the observed frequency.

- *Merger.* The merger phase begins when the orbital radius becomes smaller than the ISCO and ends with the actual merge of the two objects.
  In general, it is possible to define the energy fraction ϵ of the initial system emitted in GWs during the merger phase as

$$M_f = (1-\epsilon)M_t \tag{5.12}$$

  where M_f is the mass of the final BH, after the merger. Normally ϵ assumes values around ~ 0.05.
  This phase is characterized by a uniform spectral energy density

$$\left.\frac{dE}{df_s}\right|_{\text{merger}} = \frac{16 c \mu^2 \epsilon}{M_t (f_{\text{ringdown}} - f_{\text{merger}})} \tag{5.13}$$

  up to the ringdown frequency f_r that reads as

$$f_{\text{ringdown}} = f_r = 28600 \left(\frac{M_t}{M_\odot}\right)^{-1} \text{ Hz}. \tag{5.14}$$

- *Ringdown.* During this phase the resulting black hole settles down to a stable rotating state. The emission of GWs relative to this phase consists in a superposition of exponentially damped sinusoids. In our work we neglected the contribute coming from this phase since it is very short and h_c decreases rapidly in a small time even for high ϱ events.

In the case of an integrated coalescence signal we can have a detection even if the instantaneous amplitude of the signal is below the noise level, since the signal is integrated over many orbits. In this case, to compute the Signal-to-Noise Ratio ϱ (1.61), what it is used is the characteristic strain

$$h_c^2(f) = 4f^2 |\hat{h}(f)|^2. \tag{5.15}$$

Following [24], we have that the characteristic strain amplitude of a inspiraling and merging event reads as

$$h_c(f) = \sqrt{2}\frac{1+z}{\pi d_L(z)}\sqrt{\frac{dE}{df_s}}, \tag{5.16}$$

where $f_s = (1+z)f$ is again the gravitational wave frequency at source, $d_L(z)$ is the luminosity distance and the spectral energy density at the source reads as

$$\begin{aligned}\frac{dE}{df_s} = &\left.\frac{dE}{df_s}\right|_{\text{inspiraling}} \Theta(f_{\text{merger}} - f_s) \\ &+ \left.\frac{dE}{df_s}\right|_{\text{merger}} \Theta(f_s - f_{\text{merger}})\Theta(f_{\text{ringdown}} - f_s) \\ &+ \left.\frac{dE}{df_s}\right|_{\text{ringdown}} \Theta(f_s - f_{\text{ringdown}}),\end{aligned} \tag{5.17}$$

where Θ is the Heaviside Step function*and we neglected the ringdown contribution.

Bias

We have already addressed this issue in Section 4.1. If we suppose that we are observing coalescence between PBHs, their signals will come from low mass halos, whose bias can be expressed as [95]:

$$b_{\text{GW}} = 1 + \frac{\nu^2 - 1}{\delta_{sc}} \tag{5.19}$$

where ν and δ_{sc} are the ones defined in Section 3.2. As already said, it was calculated [96] that its value does not deviate significantly from $b_{\text{GW}} \sim 0.5$.

Magnification bias

We compute the magnification bias for GWs for the first time, since an analytic expression for it is not present in current literature. We managed to derive one, through an analogy with the case of magnification bias for galaxies, defined in Equation (4.4). For commodity we re-write its expression here:

$$s(z) = -\frac{2}{5}\left.\frac{d\log_{10} N_g(z, L > L_{\text{lim}})}{d\log_{10} L}\right|_{L_{\text{lim}}}, \tag{5.20}$$

where N_g is the (cumulative) galaxy number density per redshift and per steradian with luminosity above L_{lim}.
We observe galaxies through light, as we observe merging BHs events (and similar events) through GWs. So, if magnification of a galaxy sample can make visible some elements which were right under the luminosity visibility limit L_{lim}, on the same way cosmic magnification can make detectable GW events right under the Signal-to-Noise Ratio threshold $\varrho_{\text{lim}} = 8$.

*Heaviside Step function:

$$\Theta(x) = \begin{cases} 0 & x < 0 \\ 1 & x \geq 0 \end{cases} \tag{5.18}$$

Then, identifying the galaxy luminosity L with the GW orientation-averaged SNR $\sqrt{\langle\varrho^2\rangle}$, we defined the GW magnification bias as

$$s_{\rm GW}(z) = -\frac{2}{5}\frac{d\log_{10} N_{\rm GW}(z, \sqrt{\langle\varrho^2\rangle} > \varrho_{\rm lim})}{d\log_{10}\sqrt{\langle\varrho^2\rangle}}, \tag{5.21}$$

where the (cumulative) GW events per redshift and steradian is given by

$$N_{\rm GW}(z, \sqrt{\langle\varrho^2\rangle} > \varrho_{\rm lim}) = \begin{cases} N_{\rm GW}(z), & z \leq z_{\rm lim}, \\ 0, & z > z_{\rm lim} \end{cases} \tag{5.22}$$

Notice that this function depends only on redshift because we already integrated all other BHs merger parameters out. Therefore the magnification bias will be defined only for $z \leq z_{\rm lim}$ and is expressed as

$$s_{\rm GW}(z) = -\frac{2}{5}\frac{1}{N_{\rm GW}}\frac{dN_{\rm GW}}{dz}\left(\frac{1}{2\langle\varrho^2\rangle}\frac{d\langle\varrho^2\rangle}{dz}\right)^{-1}. \tag{5.23}$$

Since different phases of the coalescence do not share the same frequency domain, we can compute the SNR separately. The SNR for inspiraling and merger phase reads as

$$\begin{aligned} \langle\varrho^2\rangle &= \langle\varrho^2\rangle_I + \langle\varrho^2\rangle_M, \\ \langle\varrho^2\rangle_I &= \frac{2\mu M^{2/3}G^{5/3}}{15\pi^{4/3}c^3}\frac{(1+z)^{-1/3}}{\chi^2(z)}\int_{f_{\rm min}}^{f^I_{\rm up}(z)} df\frac{f^{-7/3}}{S_n(f)}, \\ \langle\varrho^2\rangle_M &= \frac{32G\mu^2\epsilon}{5\pi^2 Mc(f_r - f_m)}\frac{1}{\chi^2(z)}\int_{f^M_{\rm low}(z)}^{f^M_{\rm up}(z)} df\frac{f^{-2}}{S_n(f)}, \end{aligned} \tag{5.24}$$

where the above quantities are non-zero only if $f_{\rm min} < f^I_{\rm up}(z)$ and $f^M_{\rm low}(z) < f^M_{\rm up}(z)$, where

$$f^I_{\rm up}(z) = \min\left(f_{\rm max}, \frac{f_m}{1+z}\right), \quad f^M_{\rm low}(z) = \max\left(f_{\rm min}, \frac{f_m}{1+z}\right), \quad f^M_{\rm up}(z) = \min\left(f_{\rm max}, \frac{f_r}{1+z}\right). \tag{5.25}$$

Therefore we have that

$$\begin{aligned} \frac{d\langle\varrho^2\rangle_I}{dz} &= -\left[2\frac{\chi'}{\chi} + \frac{1}{3}(1+z)^{-1}\right]\langle\varrho^2\rangle_I + \frac{2\mu M^{2/3}G^{5/3}}{15\pi^{4/3}c^3}\frac{(1+z)^{-1/3}}{\chi^2(z)}\frac{(f^I_{\rm up}(z))^{-7/3}}{S_n(f^I_{\rm up}(z))}\frac{df^I_{\rm up}(z)}{dz}, \\ \frac{d\langle\varrho^2\rangle_M}{dz} &= -2\frac{\chi'}{\chi}\langle\varrho^2\rangle_M + \frac{32G\mu^2\epsilon}{5\pi^2 Mc(f_r - f_m)}\frac{1}{\chi^2(z)}\left[\frac{(f^M_{\rm up}(z))^{-2}}{S_n(f^M_{\rm up}(z))}\frac{df^M_{\rm up}(z)}{dz} - \frac{(f^M_{\rm low}(z))^{-2}}{S_n(f^M_{\rm low}(z))}\frac{df^M_{\rm low}(z)}{dz}\right]. \end{aligned} \tag{5.26}$$

In Figure 5.4 the shape of the magnification bias for GWs for our futuristic survey and considering one year of observation is provided.
Looking at this plot, it is natural to ask why it assumes the shown behavior. From Equation (5.23), it can be seen that this quantity is given by the fraction of two contributions: the logarithmic derivative of the events number $N_{\rm GW}$ and that of the squared SNR ϱ.

The shape of the magnification bias depends on these two factors, relating directly with the characteristics of the survey. Changing the prescription of the survey can yield very different outputs (since it would change the computation of the SNR), in a way that is not trivial, according to Equation (5.26). To show the reader how much a change in one of the survey prescription can alter the behavior of the magnification bias, we provide in Figure 5.5 this quantity for two other different values of upper frequency limits $f_{\max}$.

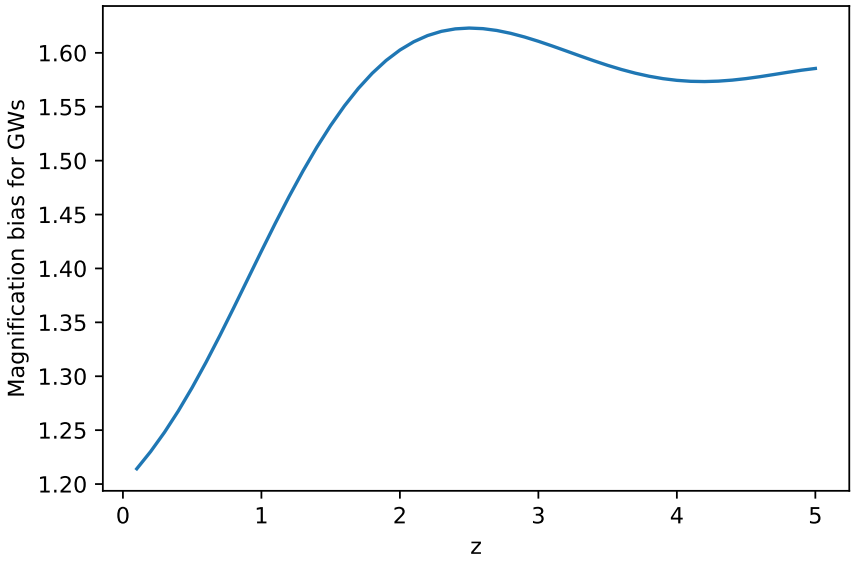

Figure 5.4: Magnification bias for our improved configuration af aLIGO, considering an observation time of 1 year.

Redshift distribution

For GWs, the number of expected events for redshift unit can be obtained from the total merger rate $\mathcal{R}_{\rm tot}(z)$ estimated in (3.3) and remembering the definition (1.30) of comoving volume [96]:

$$\frac{dN_{\rm events}}{dz} = T_{\rm obs}\frac{4\pi c\chi^2(z)}{(1+z)H(z)}\mathcal{R}_{\rm tot}(z), \tag{5.27}$$

where $T_{\rm obs}$ is the observational time, $H(z)$ is the Hubble expansion rate and $\chi(z)$ is the comoving distance. The factor $(1+z)$ arises from the fact that $\mathcal{R}_{\rm tot}(z)$, which has dimensions of a frequency, is measured at the source and we have to express it in function of the observer. From this it is possible to obtain the total number of observed events from two redshifts z_1 and z_2, considering observation of the whole sky:

$$N_{\rm events}(z) = N_{\rm GW} = T_{\rm obs}\int_{z_1}^{z_2} dz\frac{4\pi c\chi^2(z)}{(1+z)H(z)}\mathcal{R}_{\rm tot}(z). \tag{5.28}$$

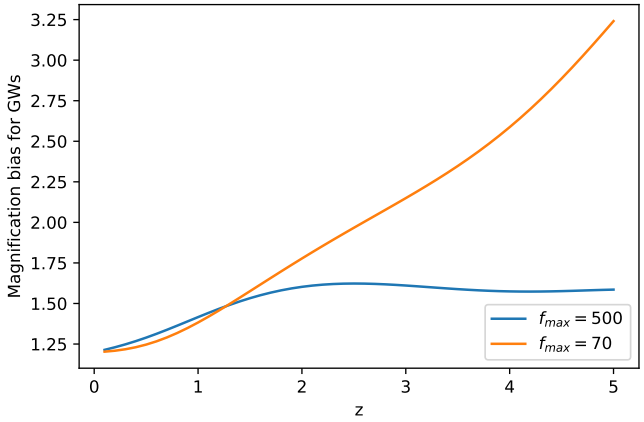

Figure 5.5: Magnification bias for our improved configuration of aLIGO, observation time of 1 year, but considering two different $f_{\max}$. It is possible to see that the variation of this parameter changes significantly the shape of the function.

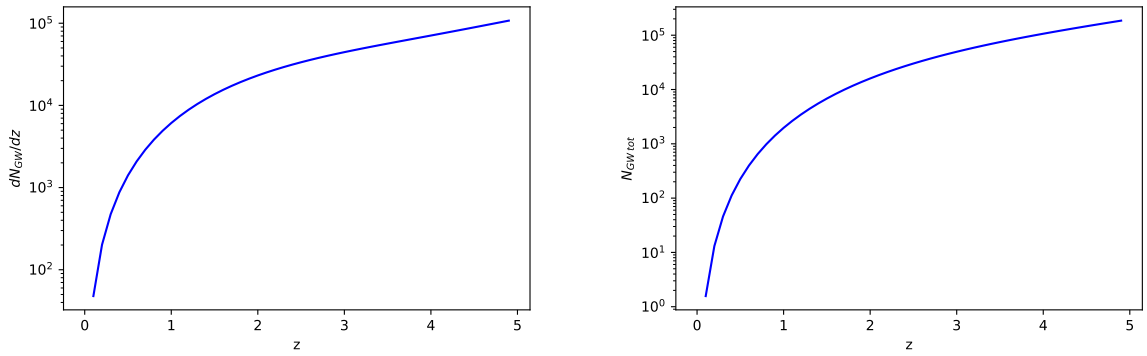

Figure 5.6: *Left*: Redshift distribution $dN_{\rm GW}/dz$ for our sample of GW events. *Right*: Cumulative number of GWs events $N_{\rm GW\,tot}$. It is the result of the integral of the redshift distribution from $z = 0$ up to a redshift z. It can be seen that increasing the redshift limit of observation increases significantly the number of observable events. Both plots regard the case of $T_{\rm obs} = 1\,yr$. Note that considering high redshifts increases significantly the total number of events, since a bigger volume is considered.

5.3 Fisher analysis

At this point we wanted to forecast if our hypothetical future survey would be able to discern the nature of progenitors of BHs mergers. As explained in Section 4.4, the Fisher analysis is the right tool to do so. It will tell us how well the cosmological parameters we consider will be measured. Obviously we are interested in the GWs bias $b_{\rm GW}$, since its value will enable us to determine from which type of halos GWs come from and, consequently, if the progenitors have stellar or primordial origins.

In our analysis we parametrize our cosmology with 6 parameters, for which we chose the following fiducial values:

- primordial power spectral index $n_s = 0.96$;
- Hubble constant $h = 0.67$;
- density parameter of cold dark matter $\Omega_{\rm cdm} = 0.26$;
- density parameter of baryonic matter $\Omega_{\rm b} = 0.05$;
- galaxy bias $b_{\rm g}$ given by Equation (5.5);
- gravitational waves bias $b_{\rm GW} = 0.5$.

We specify that we considered prescriptions of flat ΛCDM model.
After having used the CLASS code to compute the C_l with these prescriptions, we can compute the 6x6 Fisher matrix (4.17):

$$F_{\alpha\beta} = \sum_{\rm K} \sum_{l} \frac{\partial C_l^K}{\partial \theta_\alpha} \frac{\partial C_l^K}{\partial \theta_\beta} \sigma_{C_l}^{-2}, \tag{5.29}$$

where α and β are the parameters we chose and the derivatives are evaluated at their fiducial values. As said in Section 5.1, we considered three redshift bins. The K in the above expression indicates the type of auto/cross-correlation between the redshift bins $z_{1,2,3}$. To be more clear:

$$\mathrm{K} = \{1-1,\ 1-2,\ 1-3,\ 2-1,\ 2-2,\ 2-3,\ 3-1,\ 3-2,\ 3-3\} \tag{5.30}$$

where $\mathrm{K} = i - j$ means that we are considering the C_l obtained by correlating the members of the first tracer (star forming galaxies) present in the redshift bin z_i with those of the second tracer (GWs) present in the redshift bin z_j. Note that since we are considering different tracers, the situation is not symmetric: $C_l^{\rm i-j} \neq C_l^{\rm j-i}$.
For what concerns the sum over the multipoles l, the right upper limit $l_{\rm max}$ has to be find. It depends on the detector considered. We used the prescription of aLIGO, for which $l_{\rm max} = 20$.
Once we have our Fisher matrix, we can forecast the uncertainties that our survey will have in providing us the parameters estimates through Equation (4.18):

$$\varsigma_\alpha = \sqrt{(F^{-1})_{\alpha\alpha}}. \tag{5.31}$$

Specifically, we are interested in the estimate of $\varsigma_{b_{\rm GW}}$. In fact, our aim is the determine if our hypothetical future survey will be able to test the "Primordial black holes as dark matter" model. As explained in Section 5.2, the bias of GWs (coming from PBHs mergers) $b_{\rm GW}$ should be different from the one of star forming galaxies $b_{\rm g}$ (from where GWs would come if BHs were instead of stellar origin). Then, our model can be tested only if the survey will be able to measure $b_{\rm GW}$ with enough precision to make it possible to discern between the two scenarios, which means that we need:

$$\varsigma_{b_{\rm GW}} \lesssim b_{\rm GW}^{\rm stellar} - b_{\rm GW}^{\rm primordial} \sim 0.9. \tag{5.32}$$

Chapter 6

Results

Finally, in this Chapter we provide the results of our analysis.
We found out that the instrument of aLIGO would not be able to measure the bias of GW events with enough accuracy to test the "primordial black holes as dark matter" theory. In fact, as an example we considered a run of 3 years of observation (density+rsd+lensing+gr case), and it yield that the b_{GW} parameter would be estimated with an error of

$$\varsigma_{b_{\rm GW}} \sim 7 \tag{6.1}$$

which is much higher than the needed value of 0.9 from Equation (5.32). This led us to consider the improved survey described in Section 5.2.2.

Firstly, it is interesting to see if neglecting some of the effects that influence the estimate of $\Delta_{obs}(\mathbf{n}, z)$, the result of the Fisher analysis is the same. We computed the same analysis adding one more effect each time.
In Figure 6.1 we provide the results of our Fisher analysis for the three cases considered and mentioned in Section 5.1 (density+rsd, density+rsd+lensing, density+rsd+lensing+gr). For each one, we also provide three different values of the observation time of our survey: 3, 5 and 10 years. We provide also the threshold (5.32) needed to have a successful survey (i.e. to be able to infer the origins of the progenitors).
It is evident that the output changes significantly between the density+rsd case and the other two. In fact, while according to the first case the survey would not be powerful enough to test the "primordial black holes as dark matter" theory, it would indeed happen in the other two cases. Neglecting the contribute coming from the lensing part makes the Fisher prediction definitely worst (in fact, we also checked that the case density+rsd+gr gives also such a bad forecast), while considering all lensing effect yield a huge amount of additional information that permits to constrain better the GW bias estimate.
In fact, we have pointed out that because of magnification bias the number of detected counts can dramatically change. Taking into account some tracers which would be right under the threshold of detection can increase quite much the number counts. Also, size magnification can kick some of the objects out of the field of view. This is why the lensing contribute has such a strong influence: it directly affects the sources number counts.

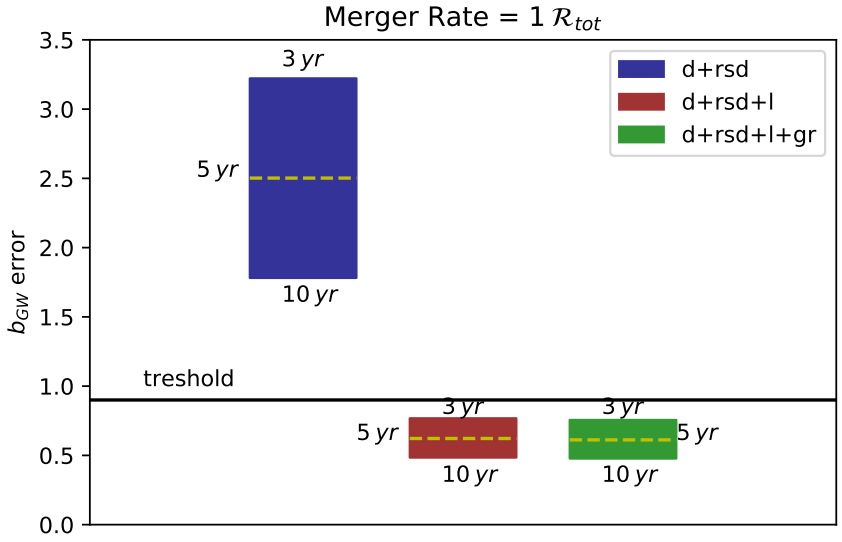

Figure 6.1: Fisher analysis forecasts for different values of observation time (3, 5, 10 years) and different contribution to the number count of sources. The abbreviations d, rsd, l, gr stand respectively for density, redshift space distortions, lensing and (general relativistic) potential terms. The threshold line corresponds to the value of $\varsigma_{b_{\rm GW}} = 0.9$. It is necessary for the bars to be below this line to succeed in determining the nature of the progenitors. Not considering lensing effects yields the worst constraints. More details are given in the text.

To visualize better this concept, in Figure 6.3 we provide the computed C_l, along with their associated errors σ_{C_l} (4.15), for two simple cases: density and density+lensing. Both of them refer to the case of an observation time of 3 years. It is evident that, in general, the calculated C_l are much closer to their errors if lensing is taken into account, yielding a smaller relative error. For a fixed error, in fact, the bigger the measure, the better the measurement is constrained. The fact that the C_l computed taking lensing into account have a smaller relative error reflects the fact that the constraining ability of the survey would be higher, as shown in Figure 6.1.
It can also be noted that, in general, the difference between the density and the density+lensing cases is more evident in the case of cross-correlations between different redshift bins. This is what we would expect: lensing is effective when one source is in front of the other.
It can also be seen that, in general, this difference (i.e. the effectiveness of the lensing) is more evident when computing star forming galaxies (i.e. more massive halos) at lower redshifts than GW events (i.e. less massive halos). In fact, we set the CLASS input so that, when considering correlations between redshift bins $i - j$, star forming galaxies and GWs belong respectively to bins i and j. So, when the lens is more massive (i.e. when the objects closer to us are heavier halos) lensing effects are more evident.
Finally, let's turn our attention in deeper detail towards the possibility to determine the

origins of merging BHs binary systems progenitors. We now consider only the complete case (density+rsd+lensing+gr) since it is the most attaining to reality. In Figure 6.2 we provide the forecasts for different observation times (3, 5 and 10 years). Since the model is based on many assumption, it might be possible that the actual merger rate estimate might be different from the expected one. To show our results in the most conservative way, we we also show how predictions would change if the total merger rate was ten times bigger or smaller than the model estimate. Firstly, we notice that, as expected, increasing

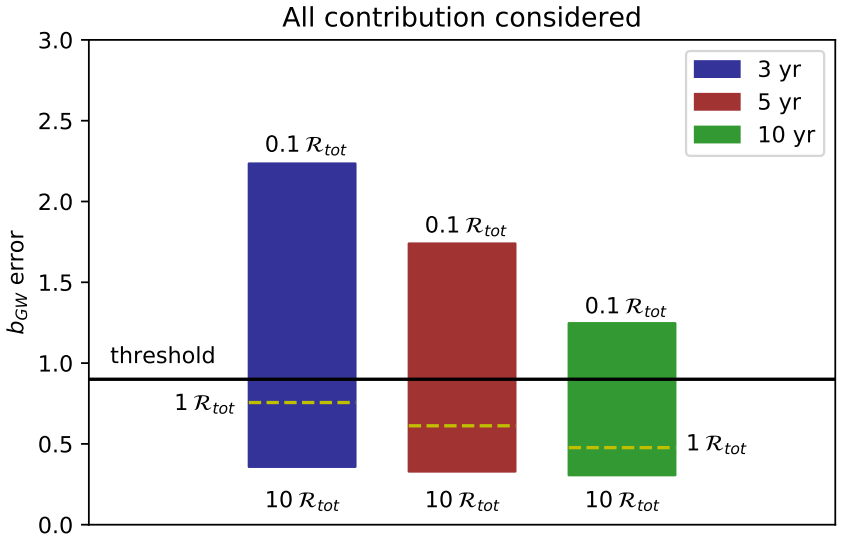

Figure 6.2: Fisher analysis forecasts for the complete case d+rsd+l+gr. Different observation times (3, 5, 10 years) are provided. It is also shown how predictions would change when taking into account uncertainties in the total merger rate $\mathcal{R}_{\rm tot}$. The threshold line corresponds to the value of $\varsigma_{b_{\rm GW}} = 0.9$. More details are given in the text.

the merger rate and increasing the observation times the results are better constrained. It can be seen that, in general, our hypotetical future survey would be able to test the "Primordial black holes as dark matter" theory in an acceptable amount of time. In fact, if the merger rate was the one the model predicts, just 3 years of observation would be enough (and obviously much less if the merger rate was 10 times bigger). On the other hand, if the merger rate was 10 times smaller, an observation period of 10 years would not be sufficient and more observation time would be required. Anyhow, this is a very conservative estimate and it could be tackled for example by improving the resolution of the instrument (i.e. l_{max}).
We also note that the threshold portrayed refers to the case where all dark matter was composed by primordial black holes. Instead, in the case were GWs came from a mixture of stellar and primordial BHs mergers, the threshold would get smaller, depending on the fraction of each component. In fact, if BHs merger came in part from stellar progenitors, the GW bias would be in between the values of 0.5 and 1.4, decreasing the distance

from the 1.4 value of star forming galaxies. Consequently, a better performance of the instrument would be needed.
In conclusion, once GW detectors will have reached the upgrades that we expect in the future, we expect to discern the nature of the BHs mergers we detect through GW experiments in an acceptable amount of time, related to the uncertainties of the model. Once it will be completed, whatever the result, we will finally be able to put constrains on this model.

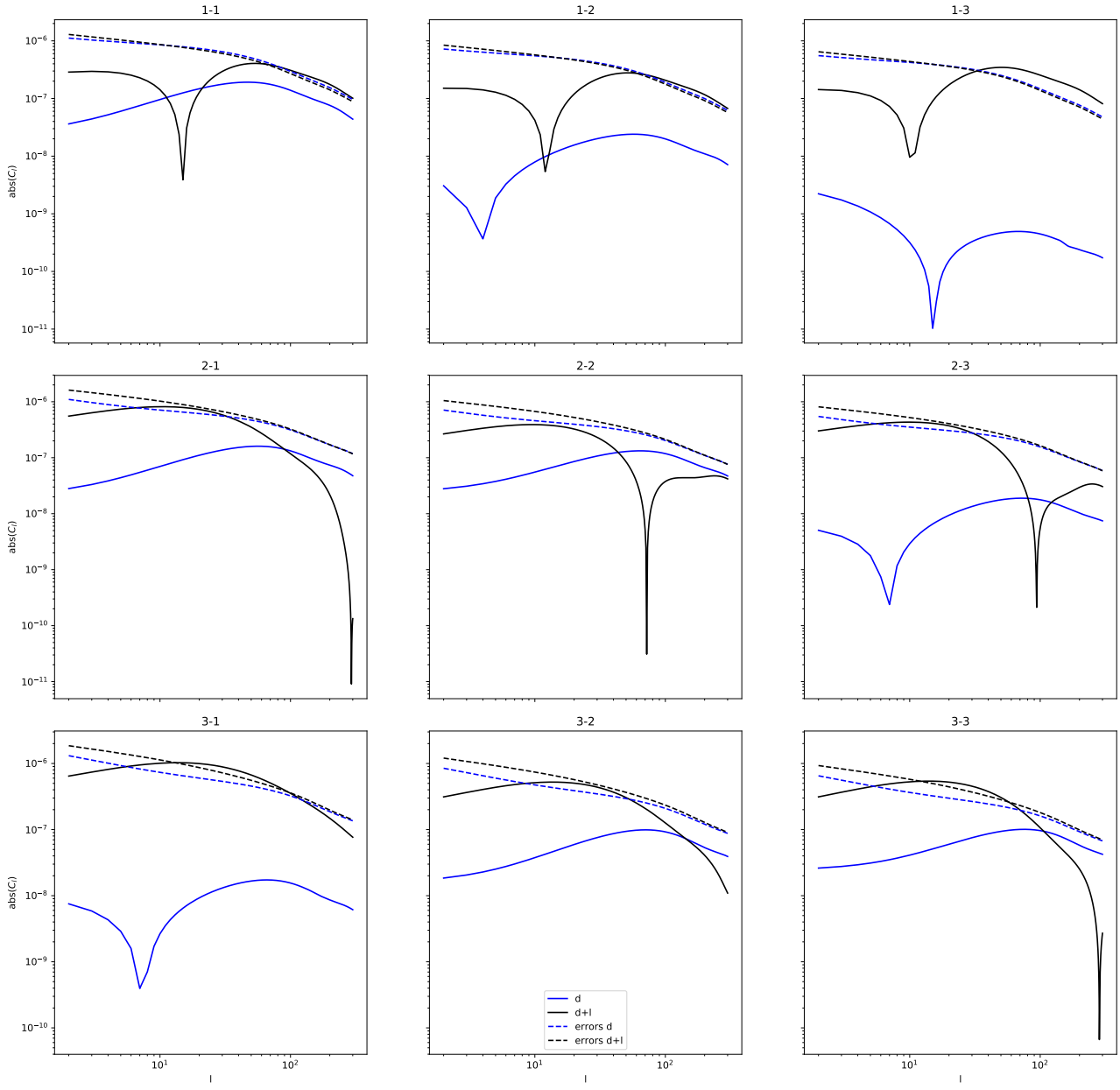

Figure 6.3: Impact of the lensing on the C_l for our futuristic survey. We show the absolute value of the computed C_l (solid lines) with errors (dashed lines) in function of the multipole l, for the two cases density (blue) and density+lensing (black). Each subplot refers to correlations between the two specific redshift bins specified in the title (for example, "1-2" means that we are considering cross-correlations between galaxies in the redshift bin z_1 and GWs in the bin z_2). As explained in the text, when taking lensing into account the relative errors on the C_l are smaller, providing a better forecast.

Chapter 7

Conclusions

Determining the nature of the dark matter is still an open and fundamental issue in physics, astrophysics and cosmology. The recent advent of gravitational wave astronomy makes it possible to study our universe in a new original way, and hopefully successfully tackle open issues like this.
Detecting mergers between black holes binary systems has recently sparked again the hypotheses about the existence of primordial black holes and the possibility that they could make up a significant fraction of the dark matter. A current popular model admits the existence of primordial black holes of a few tens of solar masses as significant components of it. These black holes would bind together, inspiral one around the other until they merge emitting gravitational waves. The frequency for these events to take place, called total merger rate, was predicted by the LIGO team and the one predicted by this model agrees with it.
This work aimed to analyze the possibility that primordial black holes actually compose dark matter and consider a method to test it. This hypothesis is strictly related to the nature of the progenitors of the mergers we detect through gravitational waves. In fact, one possible way to test this theory is to consider cross-correlations between gravitational waves events and star forming galaxies. In this way, according to where the events come from (i.e. small and obscure halos or heavy and luminous ones) it would be possible to understand the origin of the mergers progenitors (stellar or primordial).
While modeling the two tracers mentioned above, we found out that an expression for the magnification bias for gravitational waves sources (in analogy to that of luminous tracers) was not provided in literature. We derived it for the first time.
Then, to apply the cross-correlation test mentioned above, a high number of GW events is needed. In fact, to determine what type of halos mostly host the mergers we detect, we need a statistically significant amount of events. Since it is not available at present date, we established if futuristic surveys will have the capacity to accomplish this task, to check if this theory is testable trough this method.
The statistical tool that allows to predict how well a given survey will constrain some parameters is the Fisher analysis. We considered the cross-correlation power spectrum between the number counts of our two tracers, which depends on various parameters, among which there is the bias of the halos hosting the gravitational waves events we detect,

connected to the nature of the progenitors. With this method, we aimed to determine if a hypothetical future instrument will be able to measure this quantity with enough precision to succeed in establishing the validity of the "Primordial black holes as dark matter" theory.
In addition, we checked how the analysis output would change when neglecting some of the contributes that affect the source number counts, considering general relativistic effects with first order perturbation theory. They are: density, velocity, lensing and potential effects. We found out that taking into account the gravitational lensing contribute in this kind of analysis is of extreme importance, since neglecting it would produce strong alterations in the forecasts. This is what one would expect, as it directly influences the number counts of detected objects.
Finally, we obtained hopeful prevision from our Fisher analysis: in a few years of observation, near future surveys will be able to test this theory, determining whether or not the GWs we observe come from black holes of primordial origins. A period of time of three years would be sufficient if the total merger rate predicted by this theory is correct. In fact, they would measure the bias of the distribution of GWs events with a small enough uncertainty to distinguish between the heavy and light halos bias values. Once near future surveys will have the right characteristic to accomplish this aim, not only we will know more about the possible existence of primordial black holes, but we will also be able in any case to add one more piece of information to the still open issue of dark matter nature.

Bibliography

[1] S. Weinberg, *Cosmology*. Oxford University Press, 2008.

[2] **Planck Collaboration** Collaboration, P. A. R. Ade *et al.*, "Planck 2015 results - XIII. Cosmological parameters," *A&A* **594** (2016) A13.

[3] E. Hubble, "A Relation between Distance and Radial Velocity among Extra-Galactic Nebulae," *Proceedings of the National Academy of Science* **15** (1929) 168–173.

[4] C. L. Bennett, D. Larson, J. L. Weiland, and G. Hinshaw, "The 1 percent Concordance Hubble Constant," *The Astrophysical Journal* **794** no. 2, (2014) 135.

[5] P. Binétruy, "Cosmology and Gravitation: the grand scheme for High-Energy Physics,".

[6] A. M. C. Le Brun, M. Arnaud, G. W. Pratt, and R. Teyssier, "Internal dark matter structure of the most massive galaxy clusters," *Monthly Notices of the Royal Astronomical Society: Letters* **473** no. 1, (2018) L69–L73.

[7] R. Massey, T. Kitching, and J. Richard, "The dark matter of gravitational lensing," *Reports on Progress in Physics* **73** no. 8, (2010) 086901.

[8] A. Del Popolo, "Dark matter, density perturbations, and structure formation," *Astronomy Reports* **51** no. 3, (2007) 169–196.

[9] "Supersymmetric dark matter," *Physics Reports* **267** no. 5, (1996) 195 – 373.

[10] Takashi, M. Sasaki, T. Tanaka, and K. S. Thorne, "Gravitational Waves from Coalescing Black Hole MACHO Binaries," *The Astrophysical Journal Letters* **487** no. 2, (1997) L139.

[11] J. García-Bellido, A. Linde, and D. Wands, "Density perturbations and black hole formation in hybrid inflation," *Phys. Rev. D* **54** (Nov, 1996) 6040–6058.

[12] S. Bird, I. Cholis, J. B. Muñoz, Y. Ali-Haïmoud, M. Kamionkowski, E. D. Kovetz, A. Raccanelli, and A. G. Riess, "Did LIGO Detect Dark Matter?," *Phys. Rev. Lett.* **116** (May, 2016) 201301.

[13] J. B. Hartle, "Gravity: An introduction to Einstein's general relativity," *AAPT* (2003) .

[14] B. P. Abbott *et al.*, "LIGO: the Laser Interferometer Gravitational-Wave Observatory," *Reports on Progress in Physics* **72** no. 7, (2009) 076901.

[15] T. Accadia *et al.*, "Virgo: a laser interferometer to detect gravitational waves," *Journal of Instrumentation* **7** no. 03, (2012) P03012.

[16] **The KAGRA Collaboration** Collaboration, Y. Aso *et al.*, "Interferometer design of the KAGRA gravitational wave detector," *Phys. Rev. D* **88** (Aug, 2013) 043007.

[17] S. Fairhurst, "Improved source localization with LIGO-India," *Journal of Physics: Conference Series* **484** no. 1, (2014) 012007.

[18] **LIGO Scientific Collaboration and Virgo Collaboration** Collaboration, B. P. Abbott *et al.*, "GW150914: The Advanced LIGO Detectors in the Era of First Discoveries," *Phys. Rev. Lett.* **116** (Mar, 2016) 131103.

[19] B. Sathyaprakash *et al.*, "Scientific objectives of Einstein Telescope," *Classical and Quantum Gravity* **29** no. 12, (2012) 124013.

[20] H. Audley *et al.*, "Laser Interferometer Space Antenna,".

[21] B. P. Abbott *et al.*, "Observation of Gravitational Waves from a Binary Black Hole Merger," *Phys. Rev. Lett.* **116** (Feb, 2016) 061102.

[22] C. J. Moore, R. H. Cole, and C. P. L. Berry, "Gravitational-wave sensitivity curves," *Classical and Quantum Gravity* **32** no. 1, (2015) 015014.

[23] T. B. Littenberg and N. J. Cornish, "Separating gravitational wave signals from instrument artifacts," *Phys. Rev. D* **82** (Nov, 2010) 103007.

[24] E. E. Flanagan and S. A. Hughes, "Measuring gravitational waves from binary black hole coalescences. I. Signal to noise for inspiral, merger, and ringdown," *Physical Review D* **57** no. 8, (1998) 4535.

[25] B. Carr, F. Kühnel, and M. Sandstad, "Primordial black holes as dark matter," *Phys. Rev. D* **94** (Oct, 2016) 083504.

[26] Y. B. Zel'dovich and I. Novikov, "The hypothesis of cores retarded during expansion and the hot cosmological model," *Soviet Astronomy* **10** (1967) 602.

[27] S. Hawking, "Gravitationally Collapsed Objects of Very Low Mass," *Monthly Notices of the Royal Astronomical Society* **152** no. 1, (1971) 75–78.

[28] B. J. Carr and S. W. Hawking, "Black Holes in the Early Universe," *Monthly Notices of the Royal Astronomical Society* **168** no. 2, (1974) 399–415.

[29] A. Polnarev and R. Zembowicz, "Formation of primordial black holes by cosmic strings," *Phys. Rev. D* **43** (Feb, 1991) 1106–1109.

[30] S. Hawking, "Black holes from cosmic strings," *Physics Letters B* **231** no. 3, (1989) 237 – 239.

[31] U. F. Wichoski, J. H. MacGibbon, and R. H. Brandenberger, "Astrophysical constraints on primordial black hole formation from collapsing cosmic strings," *Physics Reports* **307** no. 1, (1998) 191 – 196.

[32] M. Crawford and D. N. Schramm, "Spontaneous generation of density perturbations in the early Universe," *Nature* **298** (1982) 538–540.

[33] D. La and P. J. Steinhardt, "Bubble percolation in extended inflationary models," *Physics Letters B* **220** no. 3, (1989) 375 – 378.

[34] V. Berezin, V. Kuzmin, and I. Tkachev, "Thin-wall vacuum domain evolution," *Physics Letters B* **120** no. 1, (1983) 91 – 96.

[35] J. Ipser and P. Sikivie, "Gravitationally repulsive domain wall," *Phys. Rev. D* **30** (Aug, 1984) 712–719.

[36] S. Rubin, M. Y. Khlopov, and A. Sakharov, "Primordial black holes from non-equilibrium second order phase transition,".

[37] G. Ballesteros and M. Taoso, "Primordial black hole dark matter from single field inflation," *Phys. Rev. D* **97** (Jan, 2018) 023501.

[38] M. Kopp, S. Hofmann, and J. Weller, "Separate universes do not constrain primordial black hole formation," *Phys. Rev. D* **83** (Jun, 2011) 124025.

[39] B. J. Carr and T. Harada, "Separate universe problem: 40 years on," *Phys. Rev. D* **91** (Apr, 2015) 084048.

[40] C. Gundlach, "Critical phenomena in gravitational collapse," *Living Reviews in Relativity* **2** no. 1, (1999) 4.

[41] M. W. Choptuik, "Universality and scaling in gravitational collapse of a massless scalar field," *Phys. Rev. Lett.* **70** (Jan, 1993) 9–12.

[42] I. Musco, J. C. Miller, and L. Rezzolla, "Computations of primordial black-hole formation," *Classical and Quantum Gravity* **22** no. 7, (2005) 1405.

[43] I. Musco, J. C. Miller, and A. G. Polnarev, "Primordial black hole formation in the radiative era: investigation of the critical nature of the collapse," *Classical and Quantum Gravity* **26** no. 23, (2009) 235001.

[44] I. Musco and J. C. Miller, "Primordial black hole formation in the early universe: critical behaviour and self-similarity," *Classical and Quantum Gravity* **30** no. 14, (2013) 145009.

[45] S. W. Hawking, "Black hole explosions?," *Nature* **248** no. 5443, (1974) 30.

[46] M. J. Bowick *et al.*, "Axionic Black Holes and an Aharonov-Bohm Effect for Strings," *Phys. Rev. Lett.* **61** (Dec, 1988) 2823–2826.

[47] M. Sasaki, T. Suyama, T. Tanaka, and S. Yokoyama, "Primordial black holes–perspectives in gravitational wave astronomy," *Classical and Quantum Gravity* (2018) .

[48] P. Tisserand *et al.*, "Limits on the Macho Content of the Galactic Halo from the EROS-2 Survey of the Magellanic Clouds," *Astronomy & Astrophysics* **469** no. 2, (2007) 387–404.

[49] L. Wyrzykowski *et al.*, "The OGLE view of microlensing towards the Magellanic Clouds–IV. OGLE-III SMC data and final conclusions on MACHOs," *Monthly Notices of the Royal Astronomical Society* **416** no. 4, (2011) 2949–2961.

[50] K. Griest, A. M. Cieplak, and M. J. Lehner, "Experimental Limits on Primordial Black Hole Dark Matter from the First 2 yr of Kepler Data," *The Astrophysical Journal* **786** no. 2, (2014) 158.

[51] H. Niikura *et al.*, "Microlensing constraints on primordial black holes with the Subaru/HSC Andromeda observation,".

[52] M. Oguri *et al.*, "Understanding caustic crossings in giant arcs: Characteristic scales, event rates, and constraints on compact dark matter," *Phys. Rev. D* **97** (Jan, 2018) 023518.

[53] P. N. Wilkinson, D. R. Henstock, I. W. A. Browne, A. G. Polatidis, P. Augusto, A. C. S. Readhead, T. J. Pearson, W. Xu, G. B. Taylor, and R. C. Vermeulen, "Limits on the Cosmological Abundance of Supermassive Compact Objects from a Search for Multiple Imaging in Compact Radio Sources," *Phys. Rev. Lett.* **86** (Jan, 2001) 584–587.

[54] A. Barnacka, J.-F. Glicenstein, and R. Moderski, "New constraints on primordial black holes abundance from femtolensing of gamma-ray bursts," *Physical Review D* **86** no. 4, (2012) 043001.

[55] D. P. Quinn, M. I. Wilkinson, M. J. Irwin, J. Marshall, A. Koch, and V. Belokurov, "On the reported death of the MACHO era," *Monthly Notices of the Royal Astronomical Society: Letters* **396** no. 1, (2009) L11–L15.

[56] P. W. Graham, S. Rajendran, and J. Varela, "Dark matter triggers of supernovae," *Physical Review D* **92** no. 6, (2015) 063007.

[57] F. Capela, M. Pshirkov, and P. Tinyakov, "Constraints on primordial black holes as dark matter candidates from capture by neutron stars," *Phys. Rev. D* **87** (Jun, 2013) 123524.

[58] B. J. Carr and M. Sakellariadou, "Dynamical Constraints on Dark Matter in Compact Objects," *The Astrophysical Journal* **516** no. 1, (1999) 195.

[59] T. D. Brandt, "Constraints on MACHO dark matter from compact stellar systems in ultra-faint dwarf galaxies," *The Astrophysical Journal Letters* **824** no. 2, (2016) L31.

[60] Y. Ali-Haïmoud and M. Kamionkowski, "Cosmic microwave background limits on accreting primordial black holes," *Phys. Rev. D* **95** (Feb, 2017) 043534.

[61] V. Poulin, P. D. Serpico, F. Calore, S. Clesse, and K. Kohri, "CMB bounds on disk-accreting massive primordial black holes," *Phys. Rev. D* **96** (Oct, 2017) 083524.

[62] D. Gaggero *et al.*, "Searching for Primordial Black Holes in the Radio and X-Ray Sky," *Phys. Rev. Lett.* **118** (Jun, 2017) 241101.

[63] Y. Inoue and A. Kusenko, "New X-ray bound on density of primordial black holes," *Journal of Cosmology and Astroparticle Physics* **2017** no. 10, (2017) 034.

[64] **MACHO** Collaboration, C. Alcock *et al.*, "MACHO Project Limits on Black Hole Dark Matter in the 1-30 Solar Mass Range," *The Astrophysical Journal Letters* **550** no. 2, (2001) L169.

[65] C. Alcock *et al.*, "The MACHO project: microlensing results from 5.7 years of large magellanic cloud observations," *The Astrophysical Journal* **542** no. 1, (2000) 281.

[66] J. Yoo, J. Chanamé, and A. Gould, "The End of the MACHO Era: Limits on Halo Dark Matter from Stellar Halo Wide Binaries," *The Astrophysical Journal* **601** no. 1, (2004) 311.

[67] M. A. Monroy-Rodríguez and C. Allen, "The End of the MACHO Era, Revisited: New Limits on MACHO Masses from Halo Wide Binaries," *The Astrophysical Journal* **790** no. 2, (2014) 159.

[68] M. Ricotti, J. P. Ostriker, and K. J. Mack, "Effect of Primordial Black Holes on the Cosmic Microwave Background and Cosmological Parameter Estimates," *The Astrophysical Journal* **680** no. 2, (2008) 829.

[69] D. Aloni, K. Blum, and R. Flauger, "Cosmic microwave background constraints on primordial black hole dark matter," *Journal of Cosmology and Astroparticle Physics* **2017** no. 05, (2017) 017.

[70] T. S. Li *et al.*, "Farthest Neighbor: The Distant Milky Way Satellite Eridanus II," *The Astrophysical Journal* **838** no. 1, (2017) 8.

[71] N. Bellomo, J. L. Bernal, A. Raccanelli, and L. Verde, "Primordial black holes as dark matter: converting constraints from monochromatic to extended mass distributions," *Journal of Cosmology and Astroparticle Physics* **2018** no. 01, (2018) 004.

[72] J. Abadie, B. P. Abbott, *et al.*, "Search for gravitational waves from binary black hole inspiral, merger, and ringdown," *Physical Review D* **83** no. 12, (2011) 122005.

[73] B. P. Abbott *et al.*, "GW151226: Observation of Gravitational Waves from a 22-Solar-Mass Binary Black Hole Coalescence," *Phys. Rev. Lett.* **116** (Jun, 2016) 241103.

[74] B. P. Abbott *et al.*, "GW170104: Observation of a 50-Solar-Mass Binary Black Hole Coalescence at Redshift 0.2," *Phys. Rev. Lett.* **118** (Jun, 2017) 221101.

[75] B. P. Abbott *et al.*, "GW170608: Observation of a 19 Solar-mass Binary Black Hole Coalescence," *The Astrophysical Journal Letters* **851** no. 2, (2017) L35.

[76] B. P. Abbott *et al.*, "GW170814: A Three-Detector Observation of Gravitational Waves from a Binary Black Hole Coalescence," *Phys. Rev. Lett.* **119** (Oct, 2017) 141101.

[77] B. P. Abbott *et al.*, "The Rate of Binary Black Hole Mergers Inferred from Advanced LIGO Observations Surrounding GW150914," *The Astrophysical Journal Letters* **833** no. 1, (2016) L1.

[78] J. F. Navarro, C. S. Frenk, and S. D. White, "A universal density profile from hierarchical clustering," *The Astrophysical Journal* **490** no. 2, (1997) 493.

[79] S. Cole and C. Lacey, "The structure of dark matter haloes in hierarchical clustering models," *Monthly Notices of the Royal Astronomical Society* **281** no. 2, (1996) 716–736.

[80] J. F. Navarro, C. S. Frenk, and S. D. M. White, "The Structure of Cold Dark Matter Halos," *The Astrophysical Journal* **462** (May, 1996) 563.

[81] F. Prada, A. A. Klypin, A. J. Cuesta, J. E. Betancort-Rijo, and J. Primack, "Halo concentrations in the standard Λ cold dark matter cosmology," *Monthly Notices of the Royal Astronomical Society* **423** no. 4, (2012) 3018–3030.

[82] A. D. Ludlow, S. Bose, R. E. Angulo, L. Wang, W. A. Hellwing, J. F. Navarro, S. Cole, and C. S. Frenk, "The mass-concentration-redshift relation of cold and warm dark matter haloes," *Monthly Notices of the Royal Astronomical Society* **460** no. 2, (2016) 1214–1232.

[83] Y.-Y. Mao, L. E. Strigari, R. H. Wechsler, H.-Y. Wu, and O. Hahn, "Halo-to-halo Similarity and Scatter in the Velocity Distribution of Dark Matter," *The Astrophysical Journal* **764** no. 1, (2013) 35.

[84] W. H. Press and P. Schechter, "Formation of galaxies and clusters of galaxies by self-similar gravitational condensation," *The Astrophysical Journal* **187** (1974) 425–438.

[85] J. Tinker, A. V. Kravtsov, A. Klypin, K. Abazajian, M. Warren, G. Yepes, S. Gottlöber, and D. E. Holz, "Toward a Halo Mass Function for Precision Cosmology: The Limits of Universality," *The Astrophysical Journal* **688** no. 2, (2008) 709.

[86] R. M. O'Leary, B. Kocsis, and A. Loeb, "Gravitational waves from scattering of stellar-mass black holes in galactic nuclei," *Monthly Notices of the Royal Astronomical Society* **395** no. 4, (2009) 2127–2146.

[87] G. D. Quinlan and S. L. Shapiro, "Dynamical evolution of dense clusters of compact stars," *The Astrophysical Journal* **343** (Aug, 1989) 725–749.

[88] H. Mouri and Y. Taniguchi, "Runaway Merging of Black Holes: Analytical Constraint on the Timescale," *The Astrophysical Journal Letters* **566** no. 1, (2002) L17.

[89] M. H. Lee, "N-body evolution of dense clusters of compact stars," *The Astrophysical Journal* **418** (1993) 147.

[90] J. Binney and S. Tremaine, "Galactic Dynamics," 1987.

[91] E. Munari, A. Biviano, S. Borgani, G. Murante, and D. Fabjan, "The relation between velocity dispersion and mass in simulated clusters of galaxies: dependence on the tracer and the baryonic physics," *Monthly Notices of the Royal Astronomical Society* **430** no. 4, (2013) 2638–2649.

[92] A. Vale and J. P. Ostriker, "Linking halo mass to galaxy luminosity," *Monthly Notices of the Royal Astronomical Society* **353** no. 1, (2004) 189–200.

[93] N. Kaiser, "On the spatial correlations of Abell clusters," *The Astrophysical Journal* **284** (1984) L9–L12.

[94] J. M. Bardeen, J. Bond, N. Kaiser, and A. Szalay, "The statistics of peaks of Gaussian random fields," *The Astrophysical Journal* **304** (1986) 15–61.

[95] H. J. Mo and S. D. M. White, "An analytic model for the spatial clustering of dark matter haloes," *Monthly Notices of the Royal Astronomical Society* **282** no. 2, (1996) 347–361.

[96] A. Raccanelli, E. D. Kovetz, S. Bird, I. Cholis, and J. B. Muñoz, "Determining the progenitors of merging black-hole binaries," *Phys. Rev. D* **94** (Jul, 2016) 023516.

[97] J. Liu, Z. Haiman, L. Hui, J. M. Kratochvil, and M. May, "Impact of magnification and size bias on the weak lensing power spectrum and peak statistics," *Phys. Rev. D* **89** (Jan, 2014) 023515.

[98] F. Montanari and R. Durrer, "Measuring the lensing potential with tomographic galaxy number counts," *Journal of Cosmology and Astroparticle Physics* **2015** no. 10, (2015) 070.

[99] A. Challinor and A. Lewis, "Linear power spectrum of observed source number counts," *Phys. Rev. D* **84** (Aug, 2011) 043516.

[100] S. Camera, M. G. Santos, and R. Maartens, "Probing primordial non-Gaussianity with SKA galaxy redshift surveys: a fully relativistic analysis," *Monthly Notices of the Royal Astronomical Society* **448** no. 2, (2015) 1035–1043.

[101] A. Raccanelli, F. Montanari, D. Bertacca, O. Doré, and R. Durrer, "Cosmological measurements with general relativistic galaxy correlations," *Journal of Cosmology and Astroparticle Physics* **2016** no. 05, (2016) 009.

[102] E. Hawkins *et al.*, "The 2dF Galaxy Redshift Survey: correlation functions, peculiar velocities and the matter density of the Universe," *Monthly Notices of the Royal Astronomical Society* **346** no. 1, (2003) 78–96.

[103] N. Kaiser, "Clustering in real space and in redshift space," *Monthly Notices of the Royal Astronomical Society* **227** (1987) 1–21.

[104] J. C. Jackson, "A Critique of Rees's Theory of Primordial Gravitational Radiation," *Monthly Notices of the Royal Astronomical Society* **156** no. 1, (1972) 1P–5P.

[105] A. Raccanelli, A. Bonaldi, M. Negrello, S. Matarrese, G. Tormen, and G. De Zotti, "A reassessment of the evidence of the Integrated Sachs–Wolfe effect through the WMAP–NVSS correlation," *Monthly Notices of the Royal Astronomical Society* **386** no. 4, (2008) 2161–2166.

[106] A. R. Pullen, T.-C. Chang, O. Doré, and A. Lidz, "Cross-correlations as a Cosmological Carbon Monoxide Detector," *The Astrophysical Journal* **768** no. 1, (2013) 15.

[107] C. Bonvin and R. Durrer, "What galaxy surveys really measure," *Phys. Rev. D* **84** (Sep, 2011) 063505.

[108] E. D. Dio, F. Montanari, R. Durrer, and J. Lesgourgues, "Cosmological parameter estimation with large scale structure observations," *Journal of Cosmology and Astroparticle Physics* **2014** no. 01, (2014) 042.

[109] R. A. Fisher, "The Logic of Inductive Inference," *Journal of the Royal Statistical Society* **98** no. 1, (1935) 39–82.

[110] J. Lesgourgues, "The cosmic linear anisotropy solving system (CLASS) I: Overview,".

[111] M. J. Jarvis, D. Bacon, C. Blake, M. L. Brown, S. N. Lindsay, A. Raccanelli, M. Santos, and D. Schwarz, "Cosmology with SKA Radio Continuum Surveys,".

[112] R. J. Wilman *et al.*, "A semi-empirical simulation of the extragalactic radio continuum sky for next generation radio telescopes," *Monthly Notices of the Royal Astronomical Society* **388** no. 3, (2008) 1335–1348.

[113] A. Raccanelli, G.-B. Zhao, D. J. Bacon, M. J. Jarvis, W. J. Percival, R. P. Norris, H. Röttgering, F. B. Abdalla, C. M. Cress, J.-C. Kubwimana, S. Lindsay, R. C. Nichol, M. G. Santos, and D. J. Schwarz, "Cosmological measurements with forthcoming radio continuum surveys," *Monthly Notices of the Royal Astronomical Society* **424** no. 2, (2012) 801–819.

[114] P. Ajith, "Addressing the spin question in gravitational-wave searches: Waveform templates for inspiralling compact binaries with nonprecessing spins," *Phys. Rev. D* **84** (Oct, 2011) 084037.

Acknowledgments

I would like to thank all those people who contributed to the development of this work, directly or indirectly.

Firstly, I would like to thank Prof. Sabino Matarrese, my supervisor from the University of Padova. He was always available, helpful and gave me the possibility to accomplish this abroad experience at the Institute of Cosmos Sciences of the University of Barcelona (ICCUB). There, I met my two other supervisors: Dr. Alvise Raccanelli and Prof. Licia Verde. I would like to thank them for making me feel part of their research group during these months, for following my thesis work and for giving me the possibility to keep doing research with them after my graduation. In addition, I would like to express my gratitude to all the three of them for being interested in my future PhD possibilities, giving me useful advises, suggestions, and writing me reference letters.
This list would not be complete without thanking Nicola Bellomo, whose help was of great importance in the most difficult moments, sharing with me his knowledge and experience.

At this point, I would like to thank my parents, for always believing in me, sustaining me and encouraging me to take this path, towards which I had constantly shown strong interest.

Then, I would like to thank all of my friends: those from high school, for always making me feel warmly welcome whenever coming back to my home-city; those from university and beyond for making me understand that home is wherever you find good people.

Finally, thank you Stefano, for all the strong support you gave me during these years.